



HAL
open science

Microstructural, morphological characterization and corrosion behavior of sand cast AlSi10Cu(Fe) alloy in chloride solution

Belkacem Korichi, Nacer Zazi, Stéphanie Delbrel, Kieu Ngo, Jean Paul Chopart

► To cite this version:

Belkacem Korichi, Nacer Zazi, Stéphanie Delbrel, Kieu Ngo, Jean Paul Chopart. Microstructural, morphological characterization and corrosion behavior of sand cast AlSi10Cu(Fe) alloy in chloride solution. *Chemical Papers*, 2022, 76, pp.2947-2967. 10.1007/s11696-022-02064-9. hal-03597124

HAL Id: hal-03597124

<https://hal.science/hal-03597124>

Submitted on 21 Nov 2022

HAL is a multi-disciplinary open access archive for the deposit and dissemination of scientific research documents, whether they are published or not. The documents may come from teaching and research institutions in France or abroad, or from public or private research centers.

L'archive ouverte pluridisciplinaire **HAL**, est destinée au dépôt et à la diffusion de documents scientifiques de niveau recherche, publiés ou non, émanant des établissements d'enseignement et de recherche français ou étrangers, des laboratoires publics ou privés.

1
2
3
4
5
6
7
8
9
10
11
12
13
14
15
16
17
18
19
20

Microstructural, morphological characterization and corrosion behavior of sand cast AlSi10Cu(Fe) alloy in chloride solution

Belkacem Korichi¹, Nacer Zazi^{1*}, Stéphanie Delbrel², Kieu Ngo², Jean Paul Chopart³

¹Laboratoire de Mécanique, Structures et Energétique, Université Mouloud Mammeri de Tizi-Ouzou, Tizi-Ouzou, 15000 Algeria

²Sorbonne Université, Laboratoire Interfaces et Systèmes Electrochimiques, LISE, F-75005 Paris, France

³Universite de Reims Champagne Ardenne, LISM EA 4695 UFR SEN, BP1039, Moulin de la Housse, 51687 Reims, Cedex, France

*e-mail: zazinacer@yahoo.fr, nacer.zazi@ummtto.dz

Received [Dates will be filled in by the Editorial office]

Abstract

21

22

23 In order to examine the relationship between the microstructure and the corrosion
24 behaviour in chloride solution, the microstructure of AlSi10Cu (Fe) sand cast aluminium
25 alloy has been investigated by using different techniques including scanning electron
26 microscopy, energy dispersive spectroscopy, X-ray diffraction analysis, and electrochemical
27 measurements. The microscopic analysis and X-ray diffraction analysis show several phases
28 in addition to matrix phase, including pores and phases at nano and micro scales. The average
29 rate of micropores and nanopores is 4% and 5%, respectively. The nanoparticle size varies
30 between 20 to 150 nm. Plates and corals-like silicon eutectic, rich-Cu phase and Chinese
31 script phase ($\text{Al}_{15}(\text{Mn,Fe})_3\text{Si}_2$) have been observed. Energy dispersive spectroscopy analyses
32 show the presence of a new phase ($\text{Cu}_{61.22}\text{Zn}_{25.39}\text{Ni}_{11.85}\text{Al}_{1.54}$) and the pitting corrosion has
33 been demonstrated to be initiated at the nanopores. The electrochemical measurements
34 exhibited the effect of several elements and porosities on the corrosion kinetics that is
35 controlled by charge transfer and diffusion phenomenon. Wide passive windows, followed by
36 the breakdown of passive film and excessive dissolution, have been observed in 0.3 and 3 wt.
37 % NaCl solutions. The electrochemical measurements show a high corrosion rate which does
38 not recommend the use of this alloy in seawater.

39

40

41 **Keywords:** AlSi10Cu(Fe) cast alloy, plates-like silicon eutectic, corals-like silicon eutectic,
42 $\text{Cu}_{61.22}\text{Zn}_{25.39}\text{Ni}_{11.85}\text{Al}_{1.54}$ phases, aluminum corrosion, nanopores.

43

44

Introduction

45

46

47 Aluminum alloys are chosen as materials for construction in various fields due to their
48 low density and their high corrosion resistance (Singh and Goel 1990). The aluminum-silicon
49 alloys are economical and more lightweight due to the high quantity of silicon (Ahn et al.
50 2018). However, a high ratio of silicon in aluminum alloys can increase the cracking, the wear
51 resistance and the fluidity of these alloys. Moreover, it can minimize the shrinkage porosity
52 and reduce the melting temperature point (Ahn et al. 2018; Elzanaty 2015). Therefore, the use
53 of these alloys is limited due to the variations of their properties and their limited
54 performance, especially at high temperature (Stadler et al. 2011, 2012; Ceschini et al. 2015).

55 The mechanical properties of these alloys depend on their microstructure, their
56 chemical composition and their defects (Zamani et al. 2015; Campbell 2003; Jiang et al.
57 2014). In order to enhance their properties, some metallic elements including Mg, Cu, Fe, Ni
58 and Sr have been added in addition to the silicon. In fact, the alloys microstructure is
59 characterized by various present parts such as α -aluminum phase, primary silicon particles,
60 aluminum-silicon eutectic, intermetallics and precipitates (Tenekedjiev and Gruzleski 1990;
61 Bogdanoff et al. 2016).

62 The coral-like eutectic structure can be obtained by heat treatment or by addition of
63 low concentrations of elements such as Na, Sr, or Eu which change the silicone plate-like
64 eutectic morphology to fine and round coral-like eutectic morphology (Barrirero et al. 2019).

65 The α -aluminum phase represents the matrix of cast aluminum-silicon alloys; it
66 crystallizes in the appearance of non-faceted dendrites (Warmuzek 2004), and sometimes in
67 appearance of non-dendritic forms (Zazi 2013). Moreover, the hard primary silicon particles
68 distributed in the matrix are responsible for the good mechanical properties and the high wear
69 resistance (Elzanaty 2015). (Oya et al. 2013) showed that the intergranular corrosion
70 susceptibility increases as a function of the silicon content in the alloys.

71 Aluminum-Silicon-Magnesium alloys are polyphase materials and have good
72 properties such as excellent castability, high ductility, high strength and low thermal
73 expansion coefficient (Ahn et al. 2018; Cáceres et al. 2003). These properties explain why
74 these alloys have occupied an important position in the field of automobile applications and
75 are widely used in the production of engine components. The mechanical properties of these
76 alloys depend on the size, the shape, the distribution, the degree of modification of eutectic
77 phase, and the primary silicon particles (Ye 2003; Ma et al. 2017; Mohamed and Samuel
78 2012; Al-Hella and Kawther 2013). Moreover, the casting process plays a crucial role in the
79 microstructure and mechanical properties of these alloys (Al-Hella and Kawther 2013).

80 In Aluminum-Silicon-Magnesium cast alloys, the Mg-containing phases formed during the
81 solidification are Mg_2Si , Si eutectic crystals, and the π -Fe phase. The contents of Mg and Fe
82 in these alloys and the solidification rate determine the fractions of the β -Fe and π -Fe phases
83 and the concentration of Mg in solid solution. The π -Fe phase has a Chinese script or blocky
84 morphology and it is often formed on the β -Fe plates. The Mg_2Si phase ratio increases with
85 the Mg content in the alloys, *i.e.* from close to zero for 0.3 wt% Mg to 0.2 vol% for 0.7 wt%
86 Mg (Sjölander and Seifeddine 2010). The secondary phases, including Mg_2Si , π -Fe, β -Fe and
87 Si eutectic crystals can induce specific alloy properties, and therefore have an influence on the
88 mechanical and corrosion behavior of these materials (Dobkowska et al. 2016; Cecchel et al.

89 2017). In aqueous media, the corrosion resistance of aluminum and its alloys is provided by
90 the formation of an oxide film composed of Al_2O_3 , $\text{Al}(\text{OH})_3$ and $\text{AlO}(\text{OH})$ phases on the
91 metallic surface (Barr 1977). However, for media containing chloride ions, an extensive
92 localized attack or a uniform corrosion can be observed (Bessone et al. 1992; Munoz and
93 Bessone 1999; Allachi et al. 2010; Zazi et al. 2010). The oxide film on aluminum surface is a
94 poor electronic conductor and the cathodic reactions take place on the micron size
95 intermetallic particles, or smaller precipitate particles (Zaid et al. 2008). The silicon rich phase
96 can cause galvanic corrosion, and the porosities formed during the casting processes can
97 generate crevice corrosion (Dobkowska et al. 2016)].

98 Several authors have showed the presence of Al_2Cu phase during the solidification of
99 aluminum-silicon-copper alloys (Sjölander and Seifeddine 2010; Dobkowska et al. 2016;
100 Cecchel et al. 2017; Barr 1977; Bessone et al. 1992; Munoz and Bessone 1999; Allachi et al.
101 2010; Zazi et al. 2010; Zaid et al. 2008; Djurdjevic et al 1999; Samuel et al. 1997; Li et al.
102 2003). This phase can be found in different shapes as compact block-like phase type, eutectic
103 Al_2Cu phase type or mixture of both types. This Al_2Cu phase arises from β -Fe plate's phase
104 or on coarse eutectic Si particles phase during the end of solidification process. Other phases
105 including β - Mg_2Si , Θ - Al_2Cu , π - $\text{Al}_8\text{Mg}_3\text{FeSi}_6$, Q - $\text{Al}_5\text{Cu}_2\text{Mg}_8\text{Si}_6$, α - $\text{Al}_{15}(\text{Fe},\text{Mn})_3\text{Si}_2$ and β -
106 Al_5FeSi can also be present in the alloys (Zazi et al. 2010; Li et al. 2003; Dinnis et al. 2006).

107 Porosities are cavities which are formed during the metal solidification. They are
108 regarded to be the first defect that occurs in aluminum–silicon casting alloys (Ammar et al.
109 2008). These porosities can cause various issues such as poor mechanical properties with
110 limited strength and ductility, variable fracture toughness and crack initiation sites (Ammar et
111 al. 2008). The porosity development in solidifying aluminum–silicon casting alloys is due to
112 shrinkage resulting from volume contraction associated with the solidification, and the
113 entrapment of gas (mostly hydrogen and air) resulting from a decrease in gas solubility in the
114 solid alloy compared to the liquid (Ammar et al. 2008). The formation of microporosities
115 during the solidification of aluminum alloys is responsible for problems in the production of
116 good quality products. Moreover, the process parameters during the solidification have a
117 significant effect on the microstructural development of the alloy and determine the final
118 engineering performance of the casting. Other parameters such as dendrite segregation,
119 nature, size, distribution and morphology of precipitates and porosities have also a significant
120 influence on mechanical and chemical alloys properties (Ferreira et al. 2010; L. Kuchariková
121 et al. 2021).

122 The present work is a part of a larger research project (corrosion of AlSi cast alloys),
 123 which was performed to examine and to offer a better understanding of the influence of
 124 porosities (nano and micro size) and intermetallics on the corrosion behaviour of
 125 AlSi10Cu(Fe) sand cast alloy containing zinc and to find the relationship between the
 126 microstructures and the corrosion behaviour. The study has been achieved by investigation of
 127 microstructure of AlSi10Cu(Fe) sand cast aluminum alloy before and after two weeks of
 128 immersion in chloride solution (0.3 and 3 wt. % NaCl) at room temperature and correlation
 129 with the observed corrosion phenomenon.

130 The microstructure was investigated by using optical microscopy, scanning electron
 131 microscopy (SEM), energy dispersive spectroscopy (EDS), X-ray diffraction (XRD), and
 132 electrochemical measurements.

133

134

135 Experimental

136

137 *Materials*

138

139 The investigation materials was a hypoeutectic aluminum sand casting alloy
 140 AlSi10Cu(Fe) and the experimental samples were prepared from an industrial ingot from
 141 SNVI company (Aluminum Foundry Unit, Rouiba) Algeria.

142 The chemical composition of the alloy is shown in Table 1. The casting was carried
 143 out by gravitation in sand mold at temperatures between 700°C and 750 °C.

144

145

146 **Table 1.** Chemical composition of the elaborated AlSi10Cu (Fe) aluminum cast alloy.

147

<i>Element</i>	Al	Si	Fe	Cu	Mn	Mg	Zn	Ni	other
<i>wt. %</i>	85.40	9.53	1.21	1.25	0.91	0.51	0.65	0.29	0.25

148

149 The samples were cut into cubic form from the ingot by using a mechanical saw.

150

151 *Alloy elaboration*

152 The elaboration has been carried out by the use of melting and maintenance furnaces,
153 and casting pockets with capacities of 350 kg, 150 kg and 50 kg respectively.

154 A mixture of 160 kg of AlSi10Mg ingots with dimension of (720x100x80) mm³
155 delivered by PECHINEY added to 190 kilograms of returns (Runners, channels of casting,
156 defective and rejected parts... etc.) was melted at a temperature between 700 to 750 °C, then
157 cleaning and creaming were carried out, afterwards the liquid mass was subjected to a
158 degassing treatment, and finally the liquid metal was cast in the maintenance furnace at
159 750°C, where the refining operation and a second cleaning were performed. 15 kg of the
160 liquid metal has been cast in a casting pocket and then in sand moulds. The obtained ingot
161 was in dimension (300x100x60) mm³. No chemical composition correction, in the liquid
162 mass, has been done during sand cast alloy elaboration.

163

164 ***Sample preparation and microstructure characterization***

165

166 Metallographic observations were performed using optical microscopy. The samples
167 were prepared by means of the standard metallographic procedure as following: the samples
168 were polished with emery paper from 600 to 4000 grit, then degreased with ethanol (from
169 SIGMA ALDRICH Company, with purity $\geq 99.8\%$), cleaned with distilled water, and finally
170 dried in air. The etching process was performed in the solution composed of 99.9 in wt. %
171 H₂O (Monodistilled) and 0.1 in wt. % NaOH (from SIGMA ALDRICH company, and purity
172 $\geq 98.8\%$).

173 The sample surfaces were observed by optical microscopy and scanning electron
174 microscopy before and after immersion during two weeks in aerated chloride solution of 0.3
175 wt. %. Microstructural analyses of the samples were carried out using a metallurgical
176 microscopy (Carl Zeiss ICM405 microscopy) and a scanning electron microscopy (FEG Zeiss
177 Ultra 55) equipped with an energy dispersive spectrometer EDS (Brüker EDS Quantax).

178 The X-ray diffractograms of the materials were determined by XPERT PRO X-ray
179 diffractometer at ambient temperature. The analyses of diffractograms (identification of
180 aluminum peaks and intermetallic phases) were made by means of High Score software.

181

182 ***Electrochemical measurements techniques***

183

184 The electrochemical measurements for 1.13-cm² samples immersed in sodium
185 chloride solution 0.3 and 3 wt. % NaCl at room temperature have been carried out. Using a

186 potentiostat/galvanostat GAMRY Reference 600+ controlled by software GAMRY
187 Framework. Input current /voltage range are 60 pA to 600 pA, -24 V to +24 V respectively.

188

189 A classic three-electrode method has been used. The reference electrode was a
190 saturated calomel electrode (SCE); the auxiliary electrode was a platinum grid (3-cm²).

191 Potentiodynamic polarization tests have been undertaken with a scanning rate equal to
192 1 mV/s from -1.2 V to -0.2 V according to the reference electrode.

193 The electrochemical impedance spectroscopy measurements were carried out in a
194 frequency range from 100 kHz to 1 mHz and with a 10 mV potential modulation amplitude.
195 To obtain accurate electrochemical impedance values, integration has been performed for
196 seven cycles.

197

198

199

Results and discussion

200

201 The characterization of polished cast AlSi10Cu(Fe) aluminum alloy, both etched and
202 non-etched samples, using optical microscopy is shown in Fig. 1. As it can be observed, the
203 cast AlSi10Cu(Fe) aluminum alloy is characterized by a dendritic structure of the α -aluminum
204 solid solution phase and two forms for the aluminum-silicon eutectic (silicon plate-like
205 eutectic and coral-like eutectic). Firstly, unmodified silicon eutectic (silicon plate-like
206 eutectic) is observed as it is for industrial solidifying conditions. Secondly, a modified coral-
207 like eutectic phase is distributed over the entire sample surface with a low density as it is
208 visible in Fig. 1e. Other secondary phases in the microstructure of the aluminum alloy such as
209 rich-Cu phase and Chinese script phase $Al_{15}(Mn,Fe)_3Si_2$ have been observed (Fig. 1). In order
210 to identify the types of phases, EDS analysis has been used.

211 Micrographs of sand casting aluminum alloy AlSi10Cu(Fe) are shown in Fig. 2. For
212 all figures, presence of pores and phases has been observed at micro and nano scales. The
213 identified phases are α -Al matrix, Al-Si eutectic which appeared in the interdendritic space
214 and intermetallic compounds.

215 The observed micro and nanopores are due to hydrogen gas arising during melt casting
216 because of a low speed cooling in sand casting: hydrogen gas remains in the solidified melt in
217 pores and micro shrinkages, as described by (Michna et al. 2007). On the other hand, some
218 pores are due to the effect of iron castability in AlSi10Cu(Fe) alloy, as reported by several
219 authors (Taylor et al. 1995; Mbuya et al. 2003; Roy et al. 1996), iron may degrade the

220 castability of the alloys and an increase of iron content in alloy generates an increase of
221 porosities rate. Moreover, the formation of iron rich intermetallic phases can lead to the
222 formation of shrinkage and porosity defects (Taylor 2004; Berlanga-Labari et al. 2020). An
223 increase of iron content in alloys leads to an increase in hydrogen gas pressure in equilibrium,
224 which is related to a given rate of dissolved gas. Moreover, the iron β -Al₅FeSi phase can
225 provide pore nucleation sites (Mbuya et al. 2003; Roy et al. 1996). In our case, the mass
226 percentage of iron in the alloy is equal to 1.21 wt. % and the solubility of iron in the
227 aluminum matrix is very low, *i.e.* 0.04 wt. % at 655 °C, and less than 0.01 wt. % at room
228 temperature. As a result, several iron-rich intermetallic particles can form during
229 solidification, leading to the formation of porosities in the alloys. Other phases, Al₂Cu and
230 sludge for example, restrict pore growth and expansion (Roy et al. 1996). It should be noted
231 that the nanopores were only observed at the surface of the matrix.

232 As described in literature (Tilloy et al. 2012), the size of micro and nanoparticles and
233 the morphology of intermetallic phases depend on various parameters such as chemical
234 composition, solidification conditions and particularly heat treatment process. The used
235 AlSi10Cu(Fe) cast aluminum alloy samples have not undergone heat treatments, leading to
236 the presence of micro and nanoporosities with an average rate of 4 % and 5 %, respectively.
237 The size of the observed nanoparticles varies between 20 to 150 nm.

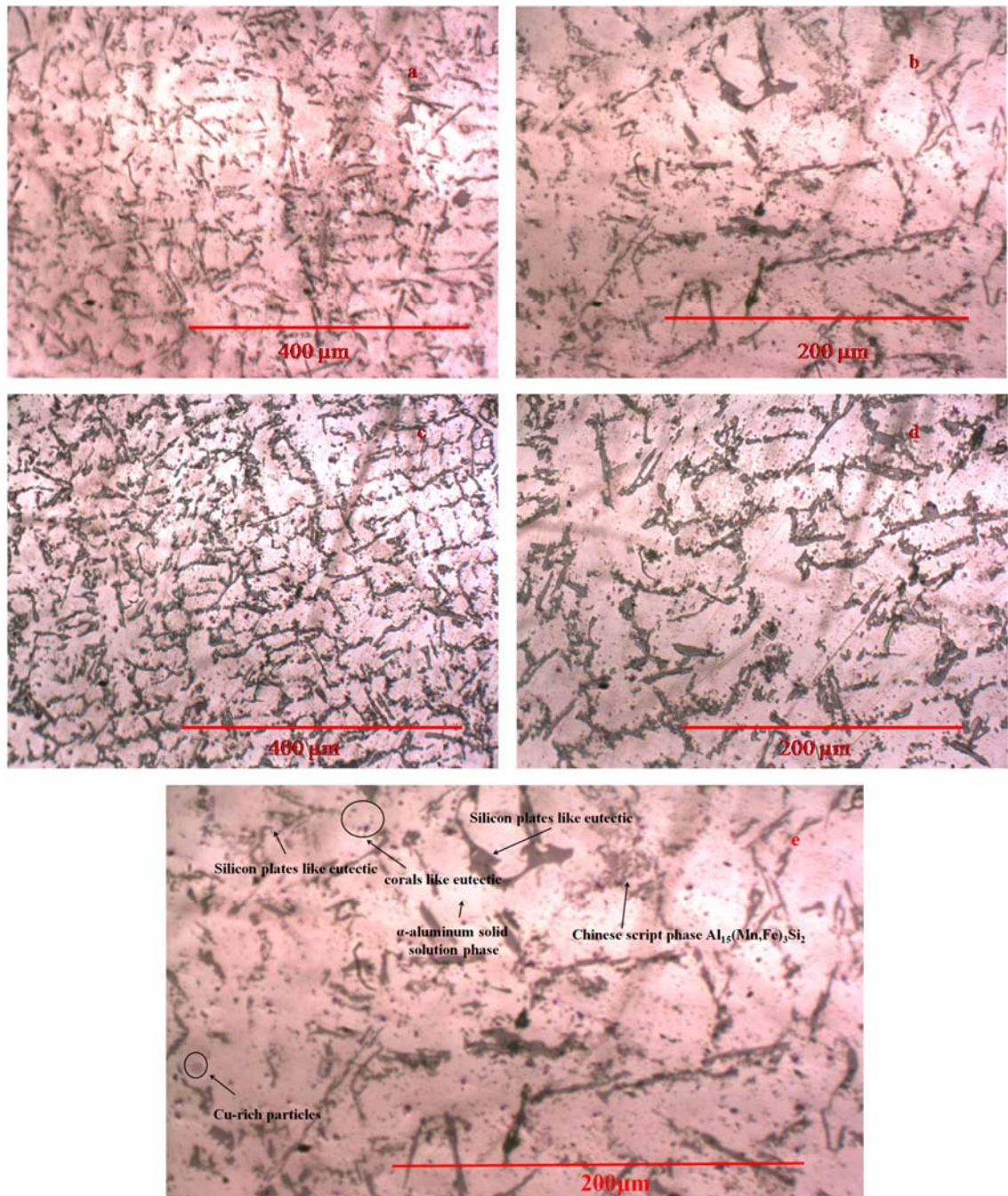
238 SEM images associated with EDS spectra and chemical composition of a polished
239 AlSi10Cu(Fe) cast aluminum alloy sample before immersion in chloride solution, for three
240 zones, are shown in Figs. 3, 4 and 5 - Tables 2, 3 and 4, respectively. These figures show the
241 matrix phase, the eutectic phase and different other secondary phases and particularly
242 numerous chemical compositions for each secondary phase. These figures and the EDS
243 spectra highlight that the samples are multicomponent aluminum alloys with various elements
244 (Al–Si–Cu–Fe–Mn–Mg–Zn–Ni). The details of chemical composition for each sample are
245 shown in Tables 2, 3 and 4.

246 According to the literature, these elements have a low solubility at room temperature
247 but in this case, their concentrations in the alloys are higher than their solubility in aluminum
248 at ambient temperature (Mathers 2002; Reardon 2011; Ambat et al. 2006; McAlister and
249 Murray 1987; Bannour et al. 2013; Skoko et al. 2009; Jia et al. 2018). It means that
250 equilibrium is not reached; these elements may also exist in supersaturated solid solutions or
251 in non-equilibrium intermetallic phases (Mathers 2002).

252 In Al-Si alloy, Al-Si multicomponent alloys or commercial and hypoeutectic alloys,
253 several phases such as Al₂Cu, Mg₂Si, α -Al₁₂(Fe,Mn)₃Si₂, β -Al₅FeSi, etc. have been reported

254 by (Mbuya et al. 2003). In this work, a new phase $\text{Cu}_{61.22}\text{Zn}_{25.39}\text{Ni}_{11.85}\text{Al}_{1.54}$ has been
 255 evidenced, as it can be observed in Fig. 4 and Table 3.

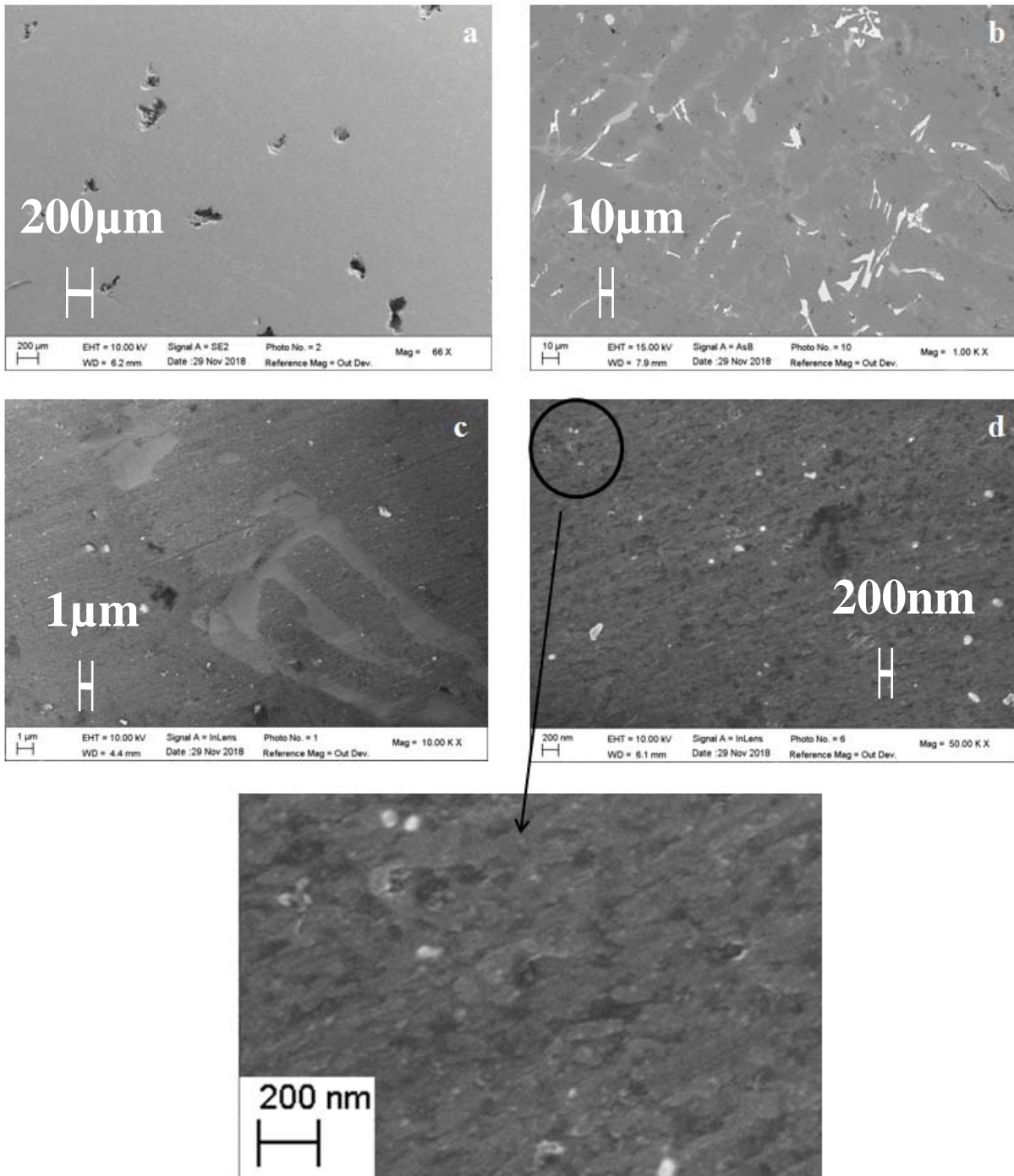
256



257

258 **Fig. 1.** Optical micrographs of AlSi10Cu(Fe) alloy: non etched sample(a-b), etched sample(c-
 259 d), zoom of fig. 1b (e).

260



261

262 **Fig. 2.** SEM images of polished, non-etched samples of AlSi10Cu (Fe) cast aluminium alloy
 263 before immersion: (a-b) micropores, (c) microphases, and (d) nanophasess and nanopores.

264

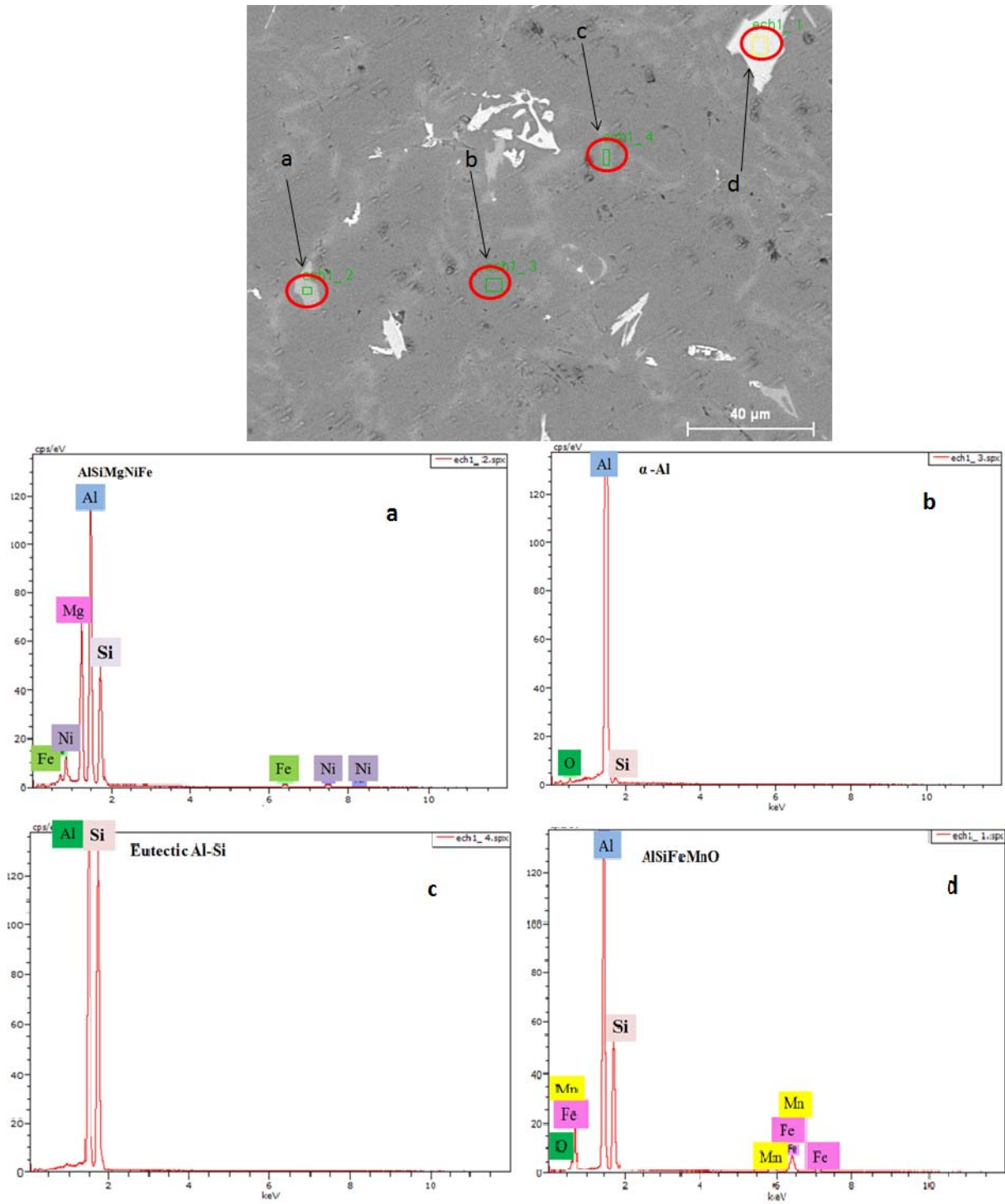
265

266

267

268

269



270

271 **Fig. 3.** SEM image and EDS spectra of points (a, b, c, and d) in zone 1 for non immersed
 272 sample.

273

274

275

276

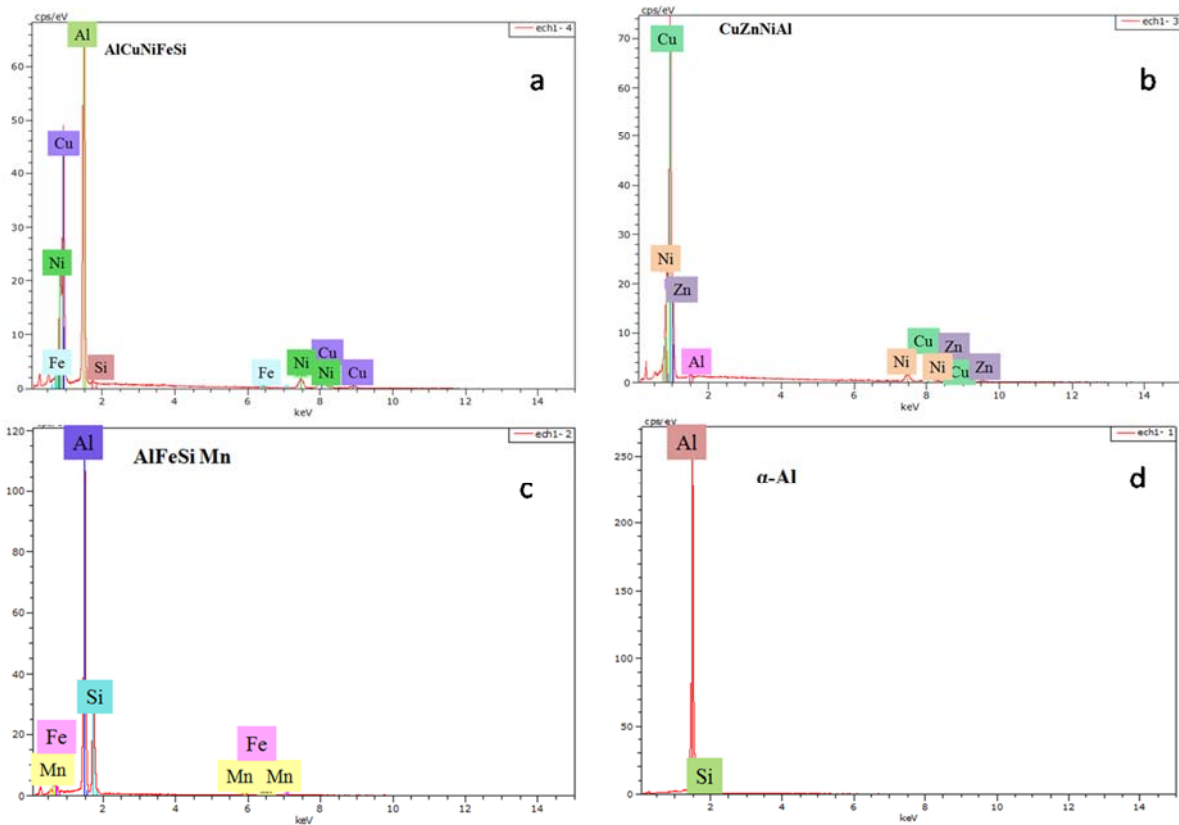
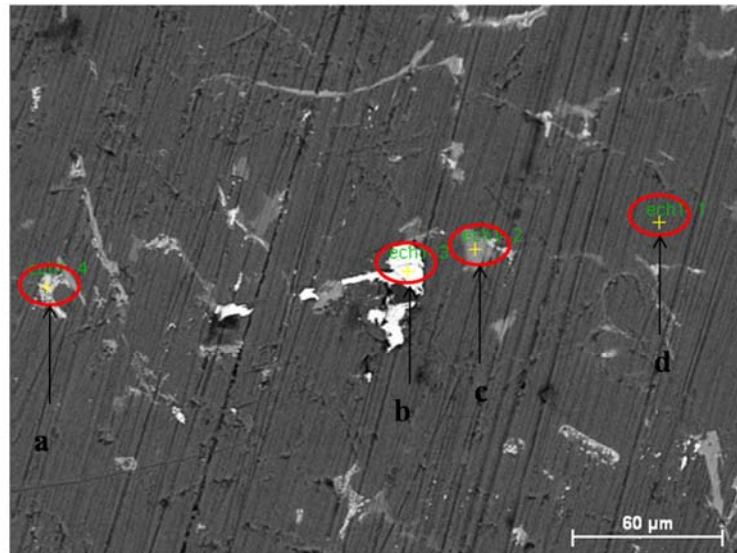
277

278 **Table 2.** EDS results, chemical compositions, for some points of non-immersed sample in zone 1

279

<i>Point a, AlSiMgNiFe</i>			<i>Points b, α-Al</i>		
<i>Element</i>	<i>wt. %</i>	<i>at. %</i>	<i>Element</i>	<i>wt. %</i>	<i>at. %</i>
Mg _k	19.37	22.69	O _k	1.80	2.99
Al _k	42.05	42.05	Al _k	96.69	95.57
Si _k	26.77	26.77	Si _k	1.51	1.43
Fe _k	3.94	3.94			
Ni _k	7.87	7.87			
<i>Total</i>	100	100	<i>Total</i>	100	100
<i>Point c, Eutectic Al-Si</i>			<i>Point d, AlSiFeMnO</i>		
<i>Element</i>	<i>wt. %</i>	<i>at. %</i>	<i>Element</i>	<i>wt.%</i>	<i>at. %</i>
Al _k	46.47	47.47	Al _k	43.87	51.89
Si _k	53.53	52.53	Si _k	26.57	30.19
			Fe _k	25.84	14.77
			O _k	0.70	1.40
			Mn _k	3.02	1.76
			<i>Total</i>	100	100
<i>Total</i>	100	100	<i>Total</i>	100	100

280



281

282 **Fig. 4.** SEM image and EDS spectra of points (a, b, c and d) in zone 2 for non immersed
 283 sample

284

285 **Table 3.** EDS results, chemical compositions, for some points of non-immersed sample in zone 2

<i>Point a, AlCuNiFeSi</i>			<i>Point b, CuZnNiAl</i>		
<i>Elements</i>	<i>wt. %</i>	<i>at. %</i>	<i>Elements</i>	<i>wt. %</i>	<i>at. %</i>
Al _k	35.40	55.73	Ni _k	11.06	11.85
Si _k	0.27	0.40	Cu _k	61.87	61.22

Ni _k	14.48	10.48	Zn _k	26.41	25.39
Cu _k	49.20	32.89	Al _k	0.66	1.54
Fe _k	0.65	0.49			
<i>Total</i>	<i>100</i>	<i>100</i>	<i>Total</i>	<i>100</i>	<i>100</i>
<i>Point c, AlSiFeMn</i>			<i>Point d, α-Al</i>		
<i>Elements</i>	<i>wt. %</i>	<i>at. %</i>	<i>Elements</i>	<i>wt. %</i>	<i>at. %</i>
Al _k	47.95	58.15	Al _k	98.09	98.16
Si _k	19.55	22.78	Si _k	01.91	01.84
Fe _k	29.28	17.16			
Mn _k	03.22	01.92			
<i>Total</i>	<i>100</i>	<i>100</i>	<i>Total</i>	<i>100</i>	<i>100</i>

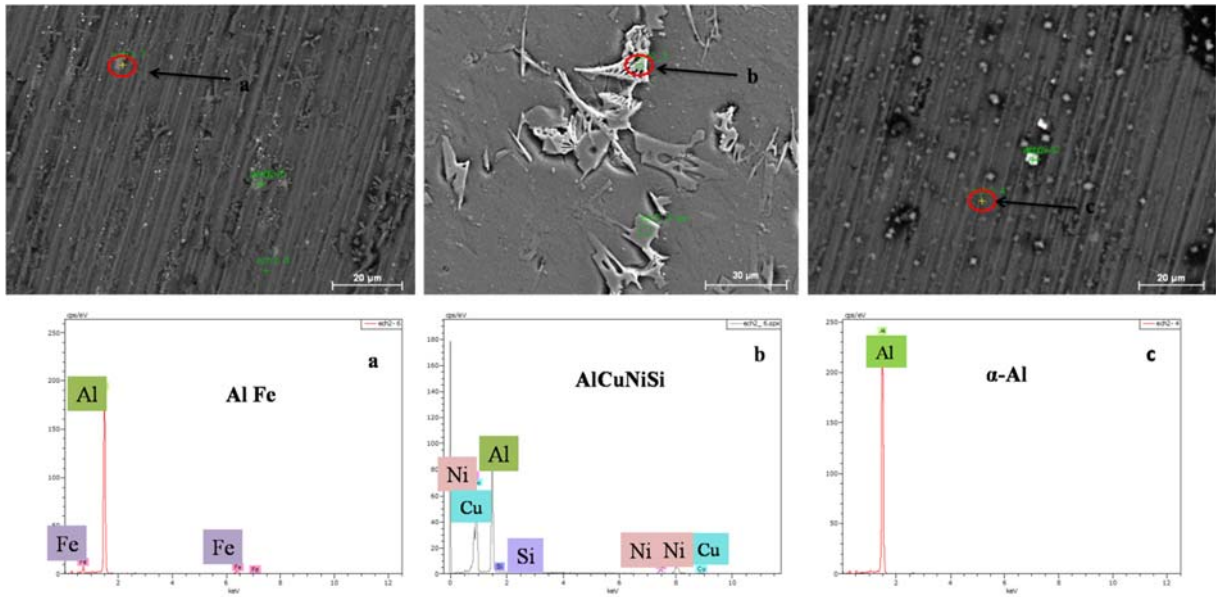
286

287

288 The Fe containing insoluble phases can take place in different forms including large or
 289 small needles or platelets, Chinese script, spheroidal or globular, rosette-like, polygonal,
 290 hexagonal, polyhedral, star-like, clusters. Other shapes can also be observed, for examples π -
 291 $\text{Al}_8\text{Mg}_3\text{FeSi}_6$ in a Chinese script morphology, Al_5FeSi as needles, $\beta\text{-Al}_5\text{FeSi}$ in platelet form,
 292 $\text{Al}_{15}(\text{Fe},\text{Mn})_3\text{Si}_2$ in polyhedron forms, $[\text{Al}_{15}(\text{Fe},\text{Mn},\text{Cr})_3\text{Si}_2]$ in sludge form (Mbuya et al. 2003;
 293 Roy et al. 1996; Taylor 2004; Tillov et al. 2012). The large number of phases, the
 294 multicomponent aspect and the differences in the composition, form, and phase size, for the
 295 aluminum-silicon alloys, does not facilitate the study of the corrosion behavior of these
 296 alloys.

297

298



299

300 **Fig. 5.** SEM image and EDS spectra of non immersed sample: (a) zone 3, (b) zone 4, (c)

301 zone 5

302

303

304 **Table 4.** EDS results, chemical compositions, for some points of non-immersed sample in zone 3

305

<i>Zone 3 (a) Al Fe</i>			<i>Zone 4(b) AlCuNiSi</i>		
<i>Elements</i>	<i>wt. %</i>	<i>at. %</i>	<i>Elements</i>	<i>wt. %</i>	<i>at. %</i>
Al _k	87.98	93.81	Al _k	38.38	58.73
Fe _k	12.02	0.49	Si _k	0.31	0.46
Total	100	100	Cu _k	44.12	28.68
			Ni	17.19	12.10
			Total	100	100
<i>Zone 5(c) alpha-Al</i>					
<i>Elements</i>	<i>wt. %</i>	<i>at. %</i>			
Al _k	100	100			
Total	100	100			

306

307

308 Fig. 6 shows the X-ray diffractogram of the aluminum AlSi10Cu(Fe) sand cast alloy.

309 The aluminum peaks are observed in the diffractogram (Fig. 6a). All seventeen phases present

310 in the alloy are shown in Fig. 6b and listed in Table 5. Three phases (7, 10 and 15) contain

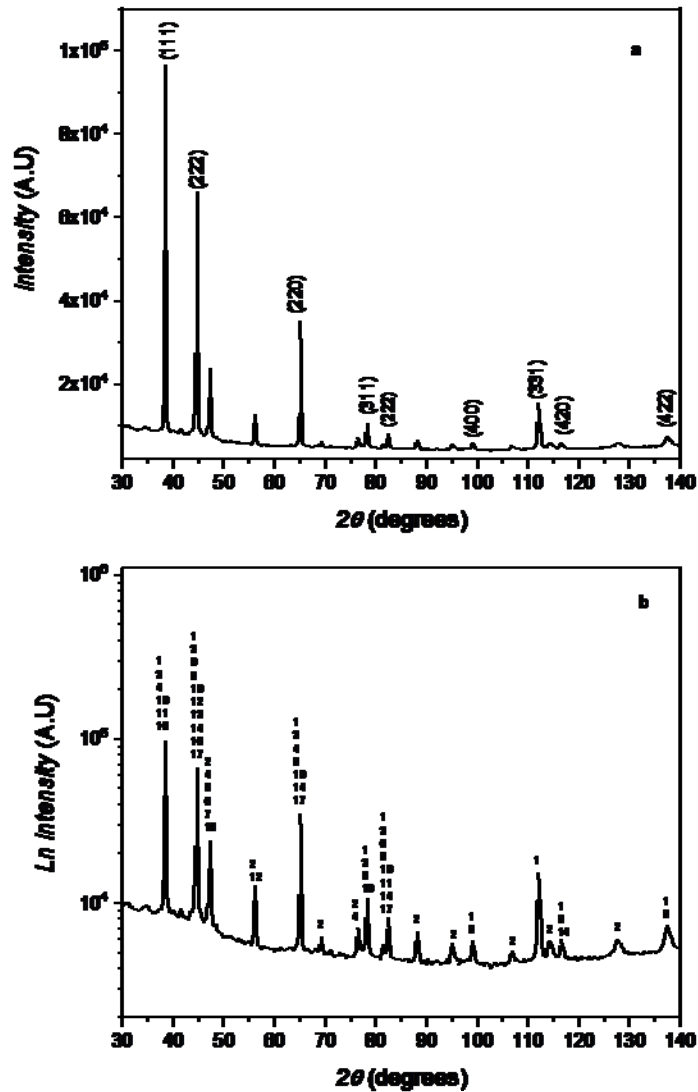
311 zinc, the phase (7) is close to the phase observed by EDS as described in Table 3 and Fig. 4,
312 which confirms the presence of the $\text{Cu}_{61.22}\text{Zn}_{25.39}\text{Ni}_{11.85}\text{Al}_{1.54}$ phase.

313 Figures 7-11 show the SEM images for several zones of AlSi10Cu(Fe) sand casting
314 aluminum alloys, immersed in 0.3 wt. % NaCl solution during two weeks. The corrosion
315 morphology of the material after immersion in chloride solution is very complex.
316 Independently of the contact between the second phases and the matrix, it seems that the
317 generalized corrosion is extended over the matrix phase, as shown in Fig. 7 (d, e), Fig. 9 (a,
318 b), Fig. 10(c, d) and Fig. 11(a-c). The presence of second phases on the surface of the alloy
319 promotes the formation of microgalvanic cells between the matrix and the second phases
320 resulting in the corrosion of the matrix surrounding the second phases (Fig. 7(d, e), Fig. 9(a,
321 b), Fig. 10(a- b) and Fig. 11(b, c, e)) or in the dissolution of second phases (Fig. 7(a-c), Fig.
322 10(c-d) and Fig. 11(b-c)). The corrosion occurring on the matrix surrounding the second
323 phases is due to the higher corrosion potential of the existing phases, as $\text{Al}_2\text{Cu}(\theta)$, AlFeMnSi,
324 AlCuFeMn, AlCuFeSi, and $(\text{Al,Cu})_x(\text{Fe,Mn})_y\text{Si}$, and the more active aluminum matrix.
325 According to the work of (Birbilis and Buchheit 2005), the cathodic nature of these
326 intermetallic phases compared to the matrix, causes the reaction of oxygen reduction on the
327 intermetallic particles surface, leading to the formation of hydroxide ions. At the same time, a
328 local increase in pH takes place, which provides a breakdown of the flimsy oxide film and the
329 dissolution of the area surrounding the intermetallic particles phases. The presence of iron,
330 copper and nickel in intermetallic phases has a determinant effect on the alloy resistance in
331 chloride solution (Ambat et al. 2006; Seri et al. 1989; Hossain et al. 2015). The dissolution of
332 intermetallic particle phases, and/or less noble segregated elements, is characterized by a
333 perforation encircled by white circles, surrounding the β -Fe plate phases, as observed in Fig.
334 11f. In this case, the dissolved intermetallic particles are less noble than the surrounded
335 phases and the matrix phases, the same phenomenon occurs between the nobler phases
336 (matrix and surrounded phases) and the dissolved phase. According to (Birbilis and Buchheit
337 2005), this can be due to the fact that the dissolved phases contain one, two or all elements
338 which are contained in the alloy, including zinc, magnesium and manganese.

339 The dissolution of the α -aluminum phase in silicon eutectic is showed in Fig. 7 (a-c), Fig.
340 10 (b-d) and Fig. 11 (a-c). This dissolution can be explained by the potential difference
341 between α -aluminum phase and silicon phase since the silicon phase potential is always
342 higher than the α -aluminum phase potential in chloride solution (Birbilis and Buchheit 2005).

343

344



345

346 **Fig. 6.** X-ray spectrum of the aluminium AlSi10Cu(Fe) sand cast alloy: (a) aluminum
 347 diffraction plans and (b) all seventeen phases in the alloy.

348

349 Fig. 9 shows the formation of several hemispherical pits in certain zones or only one pit
 350 in other zones. The authors observed also a localized corrosion with crater shape in the
 351 nanopores of the matrix phases (Fig. 8). We assume that the pit beginning occurs at nanopore
 352 level.

353

354

355

356

357

358

359 **Table 5.** Seventeen phases present in AlSi10Cu(Fe) sand cast alloy

360

<i>Phase Number</i>	<i>Chemical Formula</i>	<i>Diffraction angle 2 θ (degrees)</i>	<i>Diffraction plans (hkl)</i>
1	Al	38.47, 44.718, 65.094, 78.226, 82.431, 99.081, 112.046, 116.574, 137.463	(1 1 1), (2 0 0), (2 2 0), (3 1 1), (2 2 2), (4 0 0), (3 3 1), (4 0 0), (4 0 2)
2	Si	47.313, 56.135, 69.144, 76.395, 88.054, 94.976, 106.937, 114.124, 127.587, 136.946	(2 2 0), (3 1 1), (4 0 0), (3 3 1), (4 2 2), (5 1 1), (4 4 0), (5 3 1), (6 2 0), (5 3 3)
3	Al ₉ Si	38.498, 44.751, 56.144, 78.289, 82.701	(1 1 1), (0 0 2), (0 2 2), (1 1 3), (2 2 2)
4	Al ₈ FeMg ₃ Si ₃	38.695, 65.003, 76.322	(2 0 2), (4 0 0), (3 2 2)
5	Al ₉ Fe ₂ Si ₃	45.603, 78.780	(8 2 0), (3 5 0)
6	Al ₂ Cu	47.569, 82.352	(3 1 0), (3 2 3)
7	Ni ₇ Cu ₃ Zn ₁₀	47.359	(2 0 0)
8	Al ₉ Fe _{0.84} Mn _{2.16} Si	44,682	(2 0 3)
9	Fe ₇ Ni ₃	44.762, 65.161, 82.524, 99.198, 116.732, 137.713	(1 1 0), (2 0 0), (2 1 1), (2 2 0), (3 1 0), (2 2 2)
10	Al _{3.8} Zn _{0.2}	38.568, 44.833, 56.271, 78.451, 82.675	(1 1 1), (0 0 2), (0 2 2), (1 1 3), (2 2 2)
11	Al ₆ CuMg ₄	38.269, 82.352	(1 1 0), (0 2 2)
12	Cu _{3.17} Si	44.600	(1 0 0)
13	Al ₉ Mn ₃ Si	44.780	(0 2 3)
14	Mn ₃ Si	44.762, 65.161, 82.524, 116.732	(2 2 0), (4 0 0), (4 2 2), (6 2 0)
15	ZnNi	47.488	(0 2 2)
16	AlCu	38.853, 44.763	(3 0 0), (3 1 0)
17	Cu ₃ Si	44.537, 65.238, 82.267	(0 1 2), (0 0 3), (2 5 0)

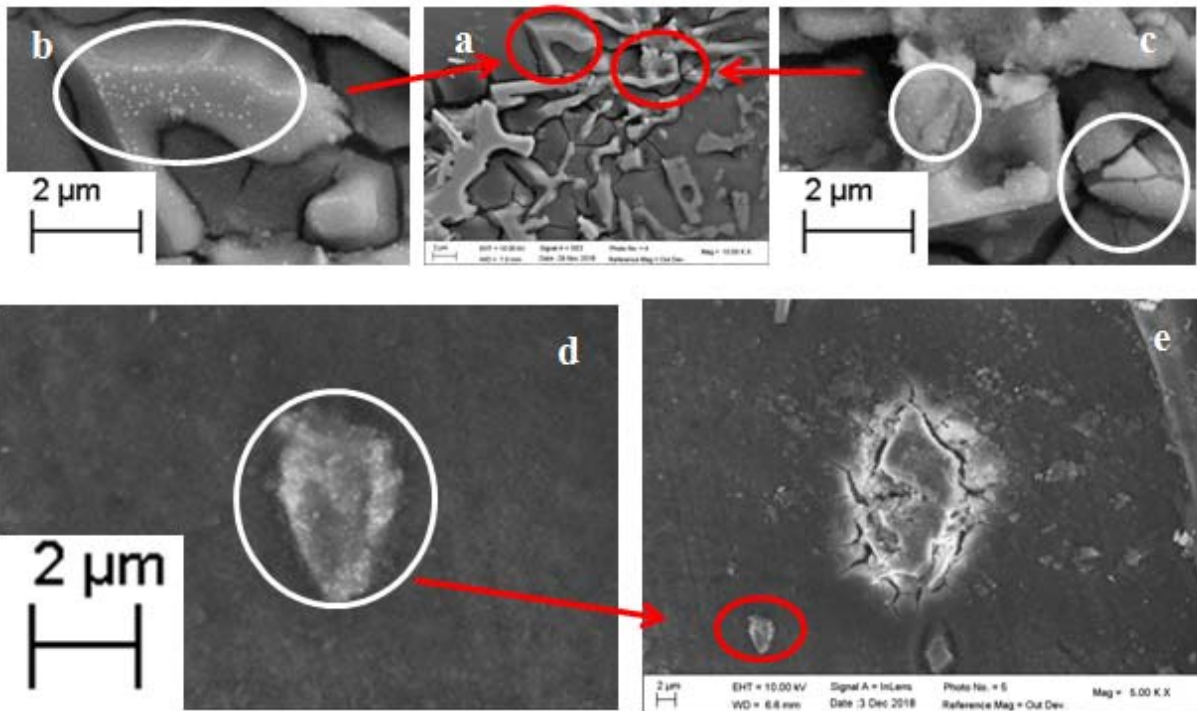
361

362

363 Small white 50-200 nm size intermetallic particles can be observed in Fig. 7 (b, c, d), Fig.
364 10 (c-d) and Fig. 11 (e-f). Particles of approximately 50 nm size were observed on the silicon
365 plates-like eutectic (Figs. 7b and 7c) and coral-like eutectic phases (Fig. 7d). These particles
366 were not dissolved after two weeks of immersion in chloride solution, meaning that their
367 corrosion potential is higher than those of all other present phases.

368

369

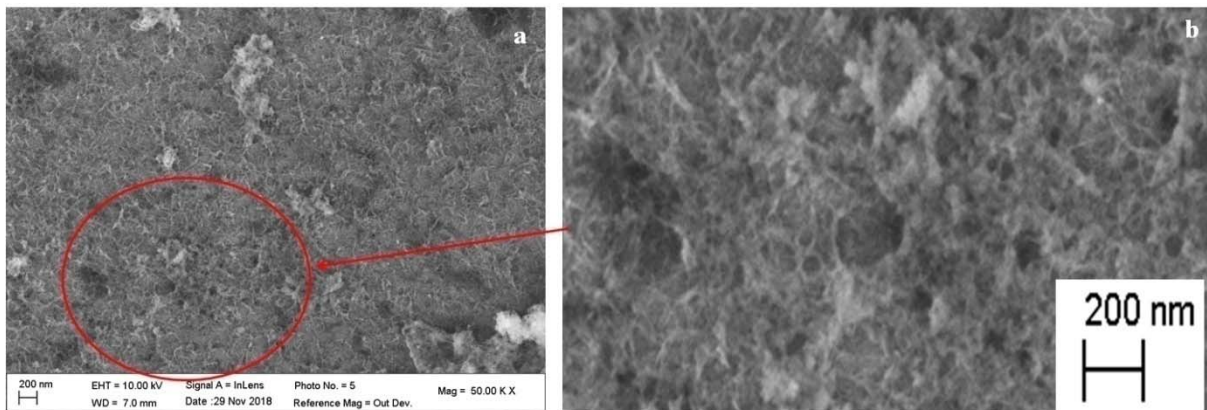


370

371 **Fig. 7.** SEM images of non-polished AlSi10Cu(Fe) sand cast aluminum alloy after two weeks
 372 of immersion in 0.3 wt. % NaCl solution (a, e). Dissolution of α -aluminum phase surrounding
 373 second phases, (b, c) magnification of SEM image presented in (a), (d) magnification of SEM
 374 image presented in (e), (b, c, d) small white intermetallic particles.

375

376



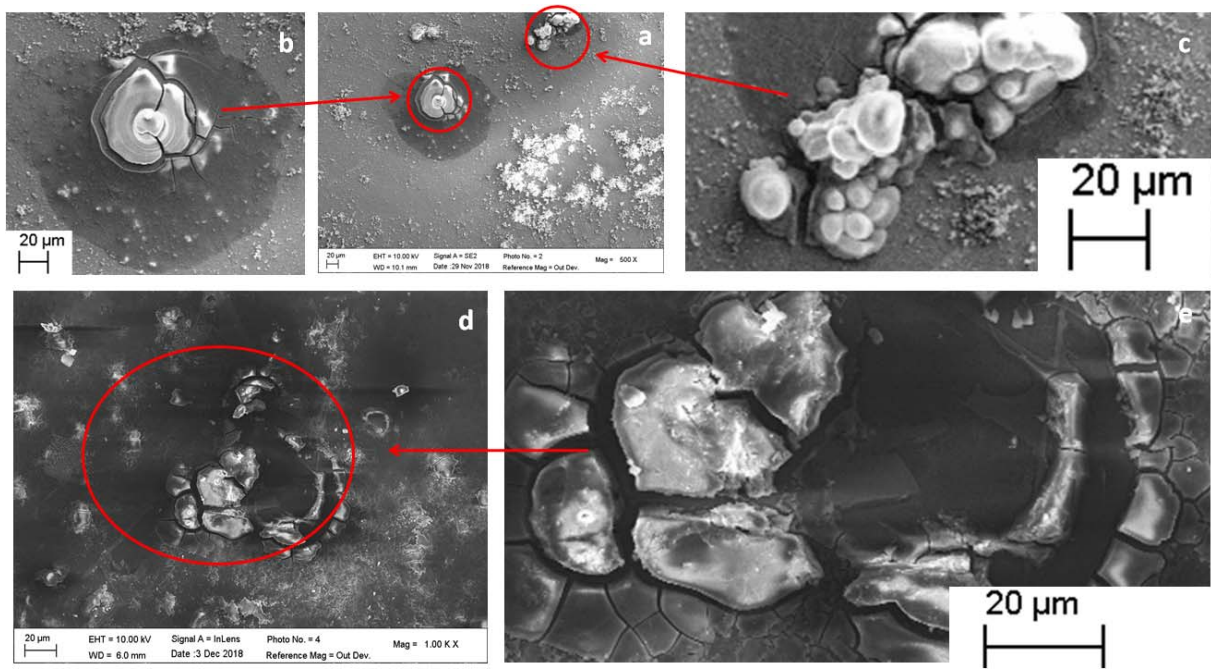
377

378 **Fig. 8.** SEM images of non-polished AlSi10Cu(Fe) sand cast aluminum alloy after 15 days of
 379 immersion in 0.3 wt. % NaCl solution: (a) corrosion presence at the nanopores, (b)
 380 magnification of SEM image presented in (a).

381

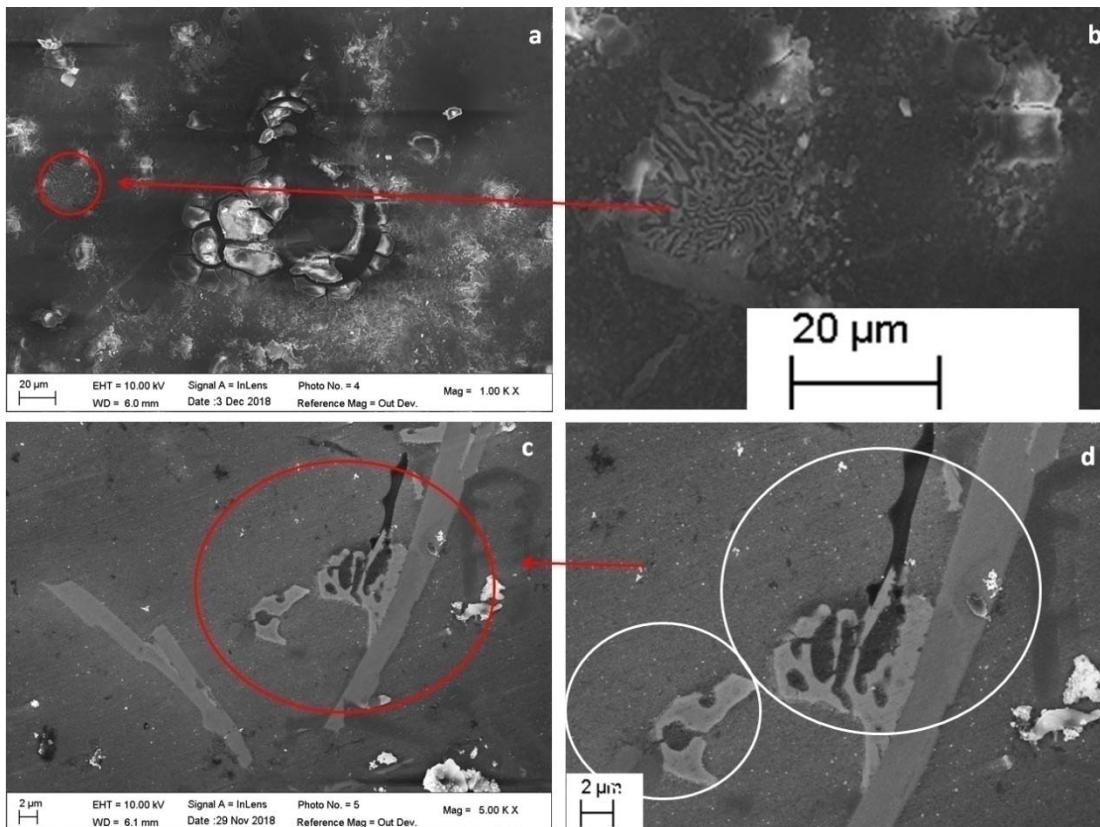
382

383



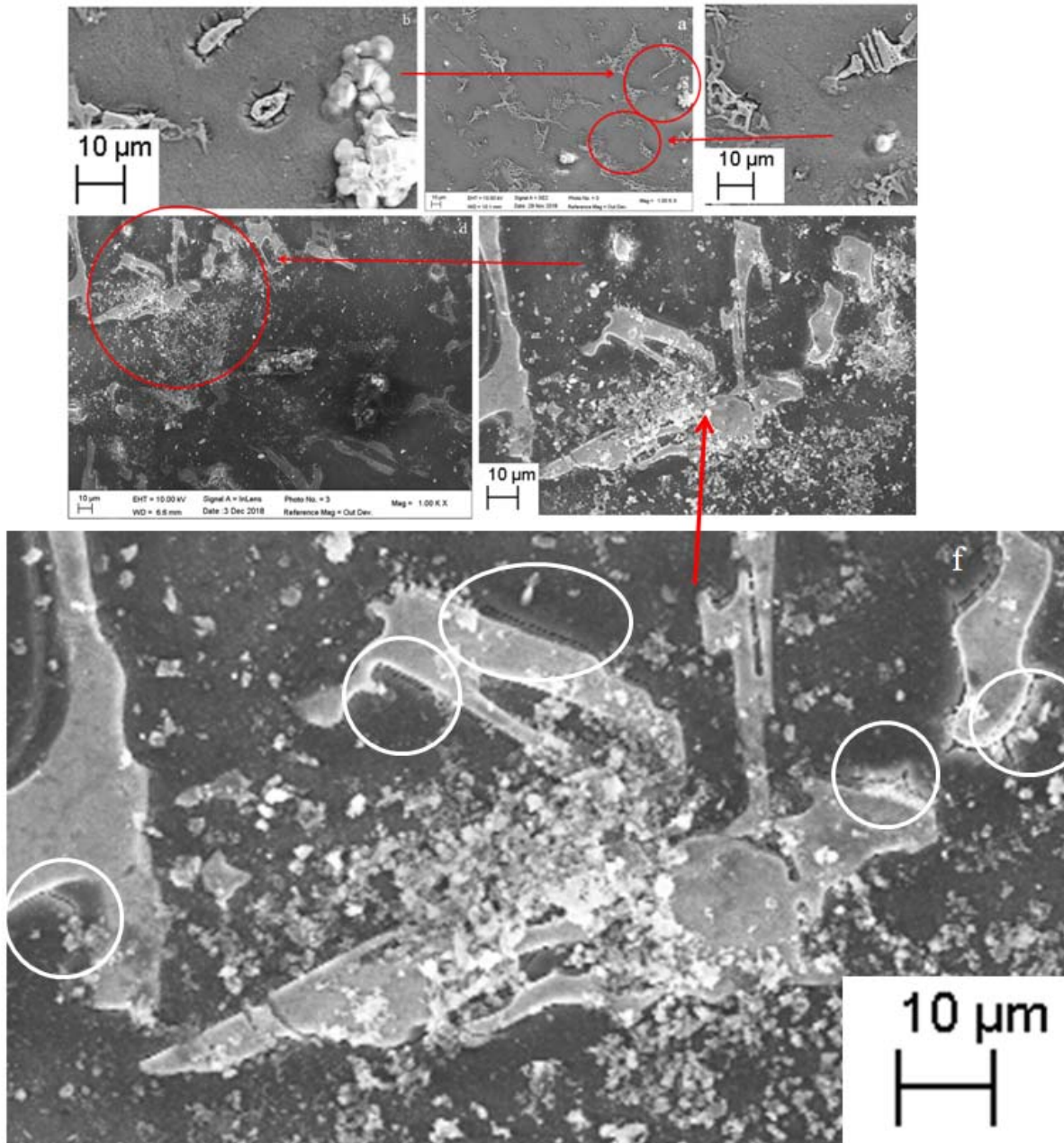
384

385 **Fig. 9.** SEM images of non-polished AlSi10Cu(Fe) sand cast aluminum alloy after two weeks
 386 of immersion in 0.3 wt. % NaCl solution: (a, d) hemispherical pits, (b, c) magnification of
 387 SEM image presented in (a), (e) magnification of SEM image presented in (d)



388

389 **Fig. 10.** SEM images of non-polished AlSi10Cu(Fe) sand cast aluminum alloy after two
 390 weeks of immersion in 0.3 wt. % NaCl solution: (a, c) dissolution of α -aluminum phase
 391 surrounding eutectic phase, (b, d) magnification of SEM image presented in (a, c).



392

393 **Fig. 11.** SEM images of non-polished AlSi10Cu(Fe) sand cast aluminum alloy after two
 394 weeks of immersion in 0.3 wt. % NaCl solution: (a, c, d) extended generalized corrosion, (b,
 395 c, e) corrosion on the matrix surrounding the second phases, (b, c, f) dissolution of second
 396 phases.

397

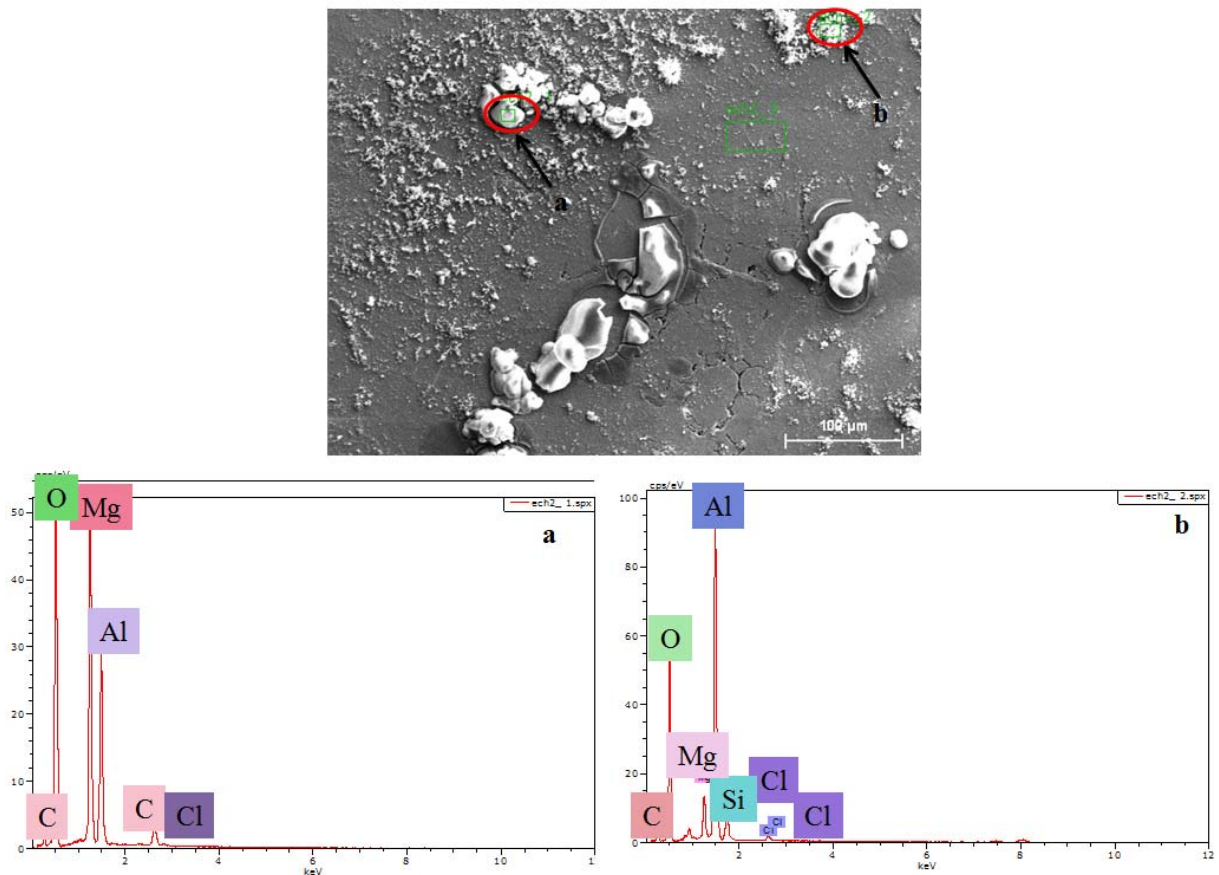
398

399 SEM images associated with EDS spectrum and chemical composition of
 400 AlSi10Cu(Fe) cast aluminum alloy after two weeks of immersion in chloride solution are
 401 shown in Fig. 12 and Table 6, respectively. Two points (a and b) in zone 6 have been chosen
 402 in the areas adjacent to the pits.

403 We observe the presence of oxygen, magnesium, aluminum, chlorine, carbon and
 404 oxygen in point a, and aluminum, silicon, magnesium and chlorine in point b. This result is in
 405 accordance with (Yoo et al. 2011). Moreover, the formation of a homogeneous layer of
 406 hydrated aluminum oxide surrounding the pit has been identified, confirming a pitting
 407 corrosion mechanism. In fact, hydrated and dehydrated aluminum oxides can be formed when
 408 aluminum is exposed to a solution containing aggressive ions, as in our case (Pourbaix 1974).
 409 The EDS analyses showed also the presence of carbon traces.

410

411



412

413 **Fig. 12.** SEM image and EDS spectra of points (a and b) in zone 6 of AlSi10Cu(Fe) sand cast
 414 aluminum alloy after two weeks of immersion in 0.3 wt. % NaCl

415

416

417 Electrochemical analyses including current-potential curves and electrochemical
 418 impedance spectroscopy of AlSi10Cu(Fe) sand cast alloy immersed in 0.3 and 3 wt. % NaCl
 419 solutions for different times are shown in Figs. 13, 14, 15, 16, 17, 18, 19 and 20 - Tables 7,
 420 8,9 and 10.

421 **Table 6.** EDS results, chemical composition, in some region of two weeks of corroded
 422 sample in 0.3 wt. % NaCl

423

<i>Point a</i>			<i>Point b</i>		
<i>Element</i>	<i>wt. %</i>	<i>at. %</i>	<i>Element</i>	<i>wt. %</i>	<i>at. %</i>
O _k	60.71	71.39	O _k	47,00	59,88
Mg _k	21.31	16.49	Mg _k	5.04	4,23
Al _k	15.46	10.78	Al _k	40.61	30.68
Cl _k	2.52	1.34	Cl _k	0.85	0.49
			Si _k	6.50	4.72
<i>Total</i>			<i>Total</i>	100	100

424

425

426 Fig. 13 shows difference in corrosion kinetics between the first hour immersion and
 427 after two weeks immersion in a 0.3 wt. % NaCl solution. A large decreasing of corrosion
 428 potential was observed, from -0.583 V after one hour- immersion to about -1.09 V after two
 429 weeks. Moreover, a weak increase of polarization resistance is observed after two weeks, i.e.
 430 from 2.5 kΩ to 2.8 kΩ (Table 7). In Figs.14 and 15, we observe a huge corrosion potential
 431 decrease from -0.583 V to -1.140 V, between 1h and 7 days immersion, followed by a
 432 corrosion potential increase up to -1.097 V after two weeks of immersion. A large increase of
 433 polarization resistance was observed between 1h and 24 h immersion, from 2.5 kΩ to 16.5
 434 kΩ, thereafter a decrease until 7 days, from 16.5 kΩ to 2.1 kΩ, and finally an increase to 2.8
 435 kΩ after 14 days (Table 7). The variations in corrosion potential and polarization resistance
 436 are due to an oxide layer formation and the dissolution of noble metals on the alloy surface.

437 The corrosion rate is determined using the following relation (Rossi et al. 2007):

438

$$439 \quad v = \frac{A i_{corr}}{n.F.\rho} \quad (1)$$

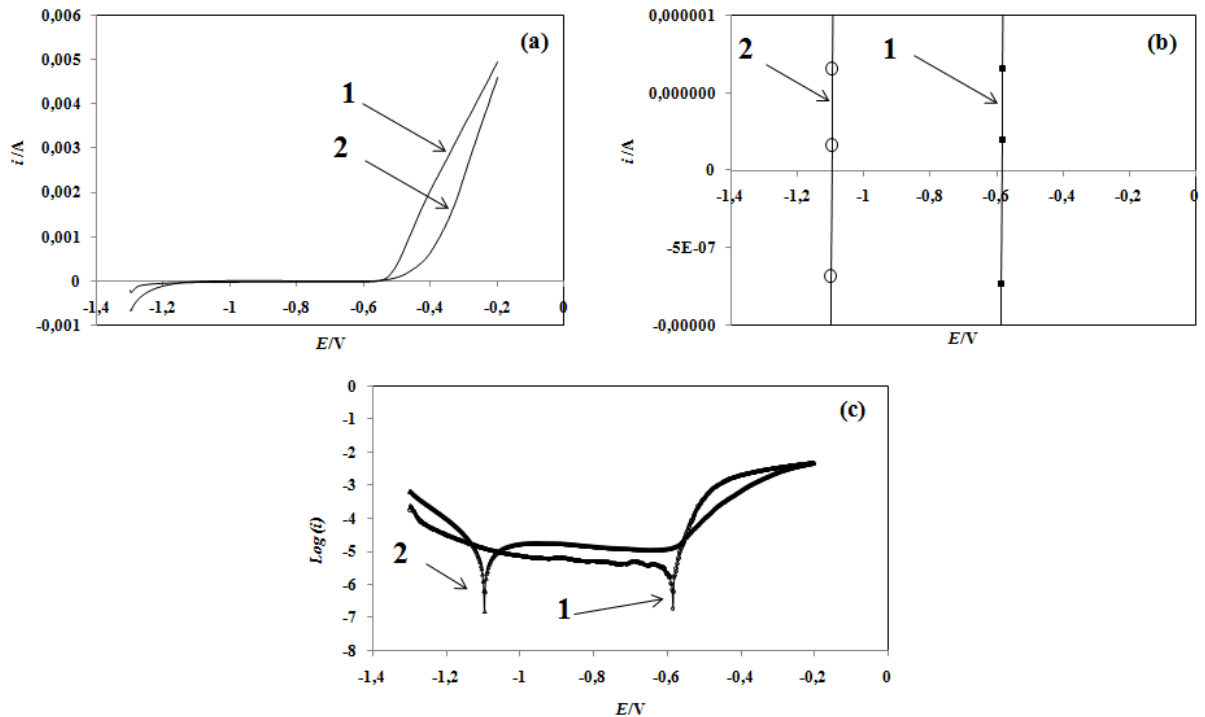
440

441 Where A is Material molar mass (g/mol.), i_{corr} Current corrosion density ($\mu\text{A}/\text{cm}^2$), n
 442 Exchanged electrons number, F Faraday constant = 96500C, ρ Density of metal (g/cm^3).

443

444 The corrosion rate increases from 0.043 mm/year after 1 h of corrosion to 0.274
 445 mm/year after 7 days immersion, and decreases to 0.172 mm/year after 2 two weeks.

446 Wide passive zones, followed by the breakdown of passive film and excessive
 447 dissolution, were observed after corrosion during three, seven days and two weeks, their
 448 values are ~570 mV, ~544 mV, ~500 mV respectively (Fig. 14).



449

450 **Fig. 13.** Polarization curves of AlSi10Cu(Fe) sand cast aluminum alloy after 1h immersion in
 451 0.3 wt. % NaCl solution (curve 1), and after 14 days of corrosion (curve 2) in 0.3 wt. % NaCl
 452 solution: (a) $i(E)$ curves, (b) magnifying effect of $i(E)$ polarization curves, and (c) $\log i(E)$
 453 curves.

454

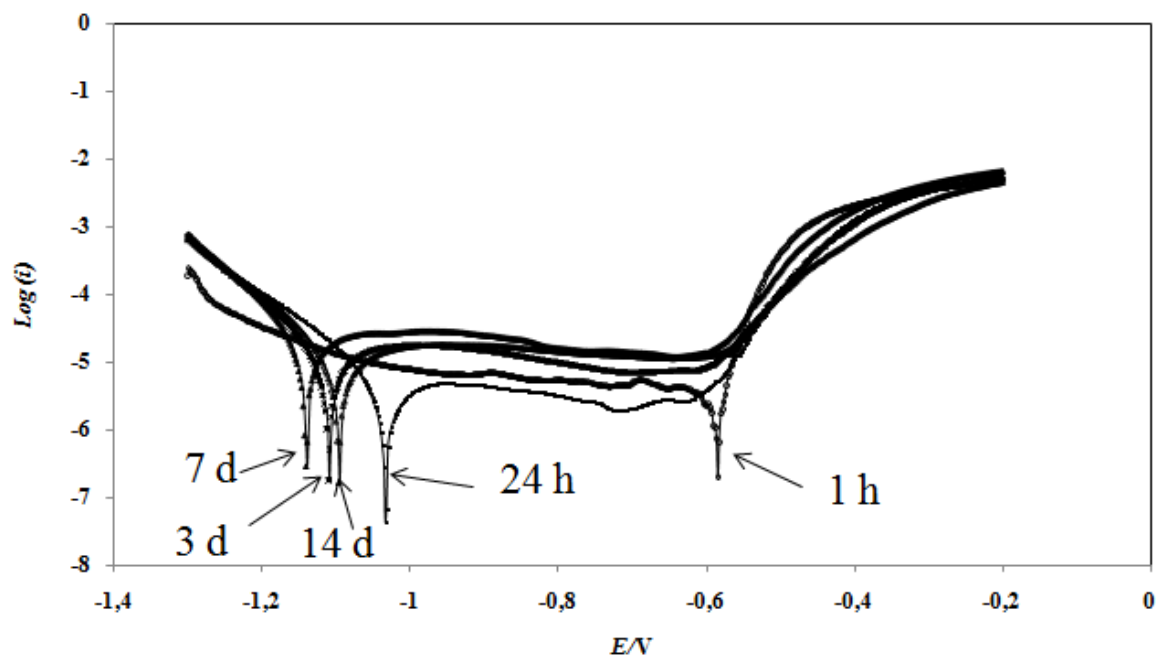
455

456 The corrosion behavior of the alloy is similar in 3 wt. % NaCl solution. Figs. 16, 17
 457 and 18 show a difference in corrosion kinetics between the first hours until two weeks of
 458 immersion. A large corrosion potential decrease is observed, from -0.935V after one hour and
 459 -1.105 V after one week, then an increase to -1.092 V after two weeks . The polarization
 460 resistance decreases from 21 k Ω after one hour of immersion to 0.5 k Ω after 3 days of
 461 corrosion, and then increases up to 1.4 k Ω after two weeks (Table 8). The corrosion rate
 462 increases from 0.017 mm/year after 1 h of immersion to 0.466 mm/year after one week. Due
 463 to this high value, the use of this alloy is not recommended for seawater.

464 The increase of NaCl concentration in the solution greatly modifies corrosion potential values
 465 and polarization resistances during the first hour of immersion. In both cases the polarization
 466 resistance is the highest at the first hour and the corrosion potential converges to the same
 467 value after two weeks of immersion. The modification of the corrosion kinetics is probably
 468 due to pitting corrosion phenomenon (Figs. 9 and 10), appearance and disappearance of

469 microporosities and nanoporosities on the surface, presence of less noble elements segregated
 470 or not and particles dissolution as function of the immersion duration.

471



472

473 **Fig. 14.** Logi(E) curves of AlSi10Cu(Fe) sand cast aluminum alloy after immersion in 0.3 wt.
 474 % NaCl solution for duration of: 1h, 24h, 3days, 7 days, and 14 days.

475

476

477 **Table 7.** Corrosion potential, polarization resistance and corrosion current of the
 478 AlSi10Cu(Fe) sand cast aluminum alloy immersed in 0.3 wt. % NaCl solution

<i>Immersion time</i>	<i>E_{corr}</i> (V/SCE)	<i>R_p</i> (kΩ)	<i>i_{corr}</i> (μA/cm ²)	<i>V_{corr}</i> (mm/year)
1h	-0.583	2.5	3.8	0.044
24h	-1.033	16.5	4.0	0.046
3days	-1.11	2.7	14.1	0.162
7days	-1.14	2.1	23.9	0.274
14days	-1.10	2.8	15.0	0.172

479

480

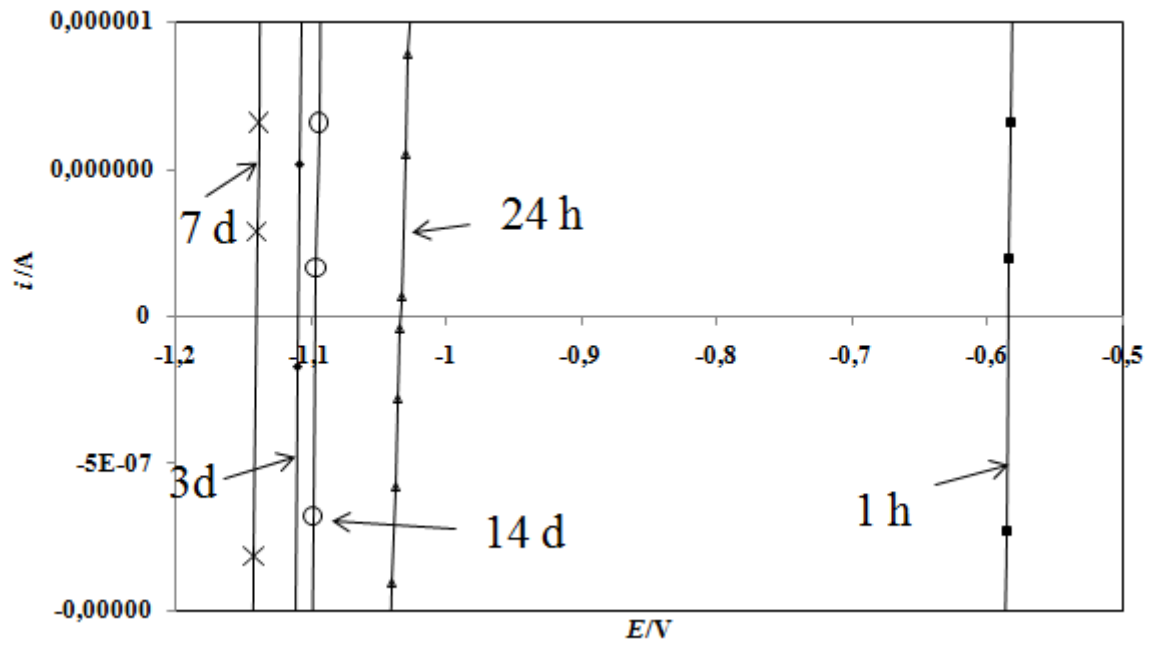
481 Wide passive windows, followed by the breakdown of passive film and excessive
 482 dissolution, were observed after twenty four hours, three days, seven days and two weeks of
 483 corrosion with values equal to ~429 mV, ~465 mV, ~493 mV, ~470 mV respectively (Fig.
 484 18).

485

486

487

488



489

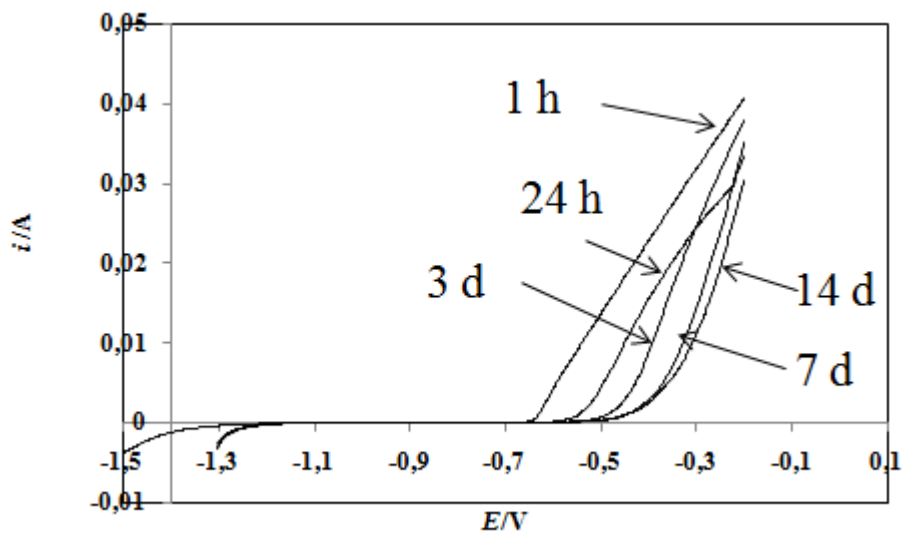
490 **Fig. 15.** Magnification of $i(E)$ curves AlSi10Cu(Fe) sand cast aluminum alloy after immersion
 491 in 0.3 wt. % NaCl solution for duration of: 1h, 24h, 3 days, 7 days, and 14 days.

492

493

494

495



496

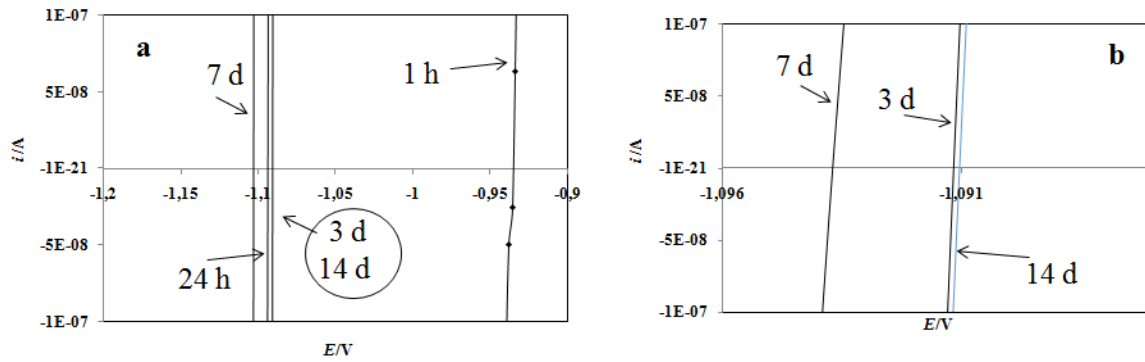
497 **Fig. 16.** $i(E)$ curves of AlSi10Cu(Fe) sand cast aluminum alloy in 3 wt. % NaCl solution after
 498 different immersion times.

499

500

501

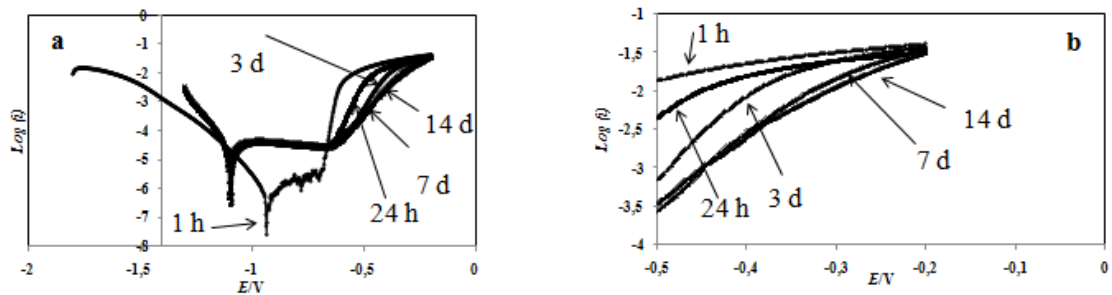
502



503

504 **Fig. 17.** Magnification of $i(E)$ curves of AlSi10Cu(Fe) sand cast aluminum alloy in 3 wt. %
 505 NaCl solution after different immersion times.

506



507

508 **Fig. 18.** Log $i(E)$ curves of AlSi10Cu(Fe) sand cast aluminum alloy in 3 wt. % NaCl solution
 509 after different immersion times.

510

511

512 **Table 8.** Corrosion potential, polarization resistance, and corrosion rate of the AlSi10Cu(Fe)
 513 sand cast aluminum alloy immersed in 3 wt. % NaCl solution

514

Immersion time	E_{corr} (V/SCE)	R_p (k Ω)	i_{corr} (μ A/cm ²)	V_{corr} (mm/year)
1h	-0.9350	21	1.5	0.017
24h	-1.0933	2.1	33	0.375
3days	-1.0917	0.5	34	0.385
7days	-1.1046	1.1	41	0.466
14days	-1.0921	1.4	34	0.385

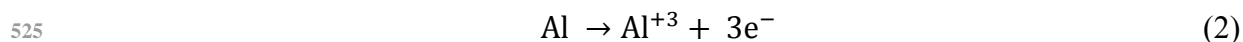
515

516

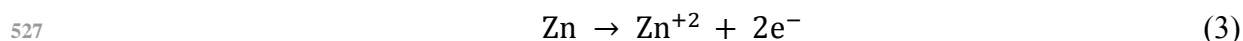
517 Fig. 19 shows the Nyquist plots of impedance of the alloy immersed in 0.3 wt. % NaCl
 518 solution. In all diagrams, a charge transfer loop at high frequency followed by a diffusion
 519 phenomenon at low frequency is observed; the result is in good agreement with (Frers et
 520 al.1990, Jafarzadeh et al. 2009 and Fernandes et al. 1989). The charge transfer loop is directly
 521 related to electrochemical transfer reactions, typically due to the metallic dissolution
 522 occurring on the alloy surface, for example:

523

524



526 And,



528

529

530 The transfer resistance value increases with immersion time, from 554 Ω after one
 531 hour to 2768 Ω after two weeks of immersion (Table 9).

532 The diffusion (Warburg) line is representative of the transport phenomenon, towards
 533 the porous surface layer of the alloy.

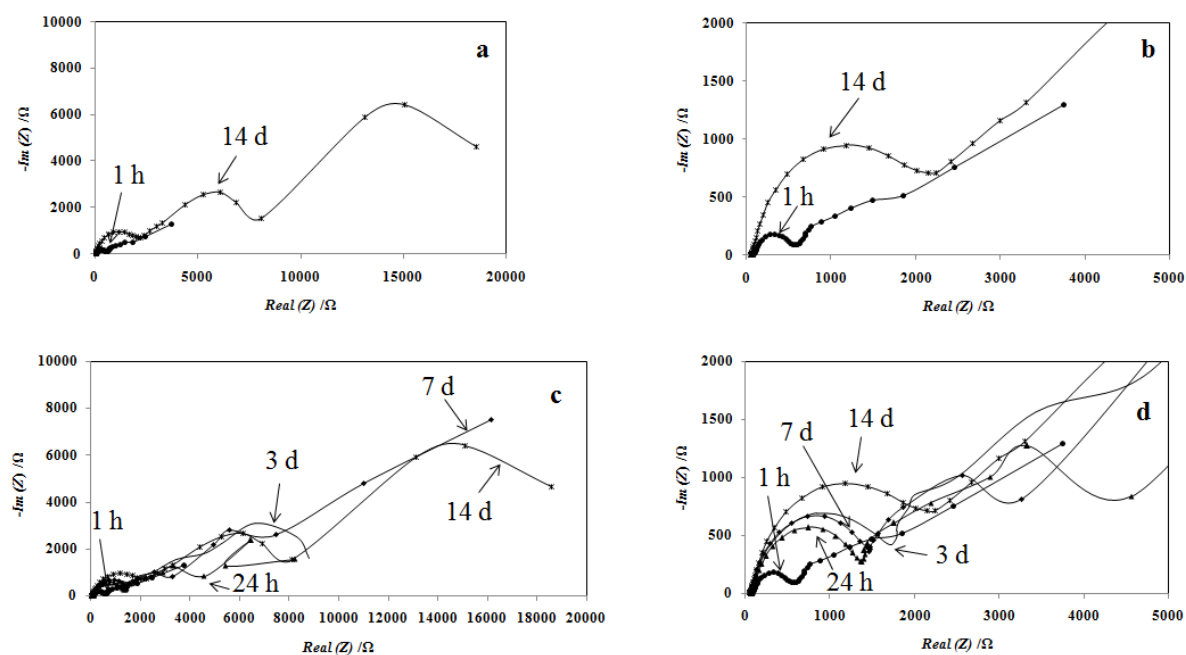
534 An analysis of the high-frequency loop allows determining the double-layer
 535 capacitance and transfer resistance values. The double-layer capacitance C_d values are not
 536 constant according to the immersion times (Table 9); this is probably due to an evolution of
 537 the passive layer thickness on the alloy surface, the localized corrosion process, and the
 538 presence of porosities. The increase of the transfer resistance value can be explained by the
 539 increase of the oxide layer thickness (Zazi et al. 2010).

540

541 The impedance spectra of AlSi10Cu(Fe) sand cast aluminum alloy immersed in 3 wt.
 542 % NaCl solution are presented in Fig. 20 and the characteristics of the impedances curves are
 543 given in Table 10. As for the previous case, the diagrams show a charge transfer loop,
 544 followed by a diffusion phenomenon. The charge transfert resistance (R_t) increases with
 545 immersion time, from 271 Ω after one hour up to 2536 Ω after two weeks of immersion.
 546 However, the double layer capacitance (C_d) values decrease from 587 μF after one hour up to
 547 323 μF after two weeks of immersion.

548

549



550

551 **Fig. 19.** (a) Nyquist plots of AlSi10Cu(Fe) sand cast aluminum alloy immersed in 0.3 wt. %
 552 NaCl solution after 1h of immersion and after 14 days of corrosion, (b) magnification of
 553 Nyquist plot of (a), (c) after different immersion times, (d) magnification of Nyquist plot
 554 of(c).

555

556

557 **Table 9.** Solution resistance (R_s), transfer resistance (R_t) and double-layer capacitance (C_d)
 558 AlSi10Cu(Fe) sand cast aluminum alloy of immersion in 0.3 wt. % NaCl versus time of
 559 immersion for sample area equal to 1 cm²

560

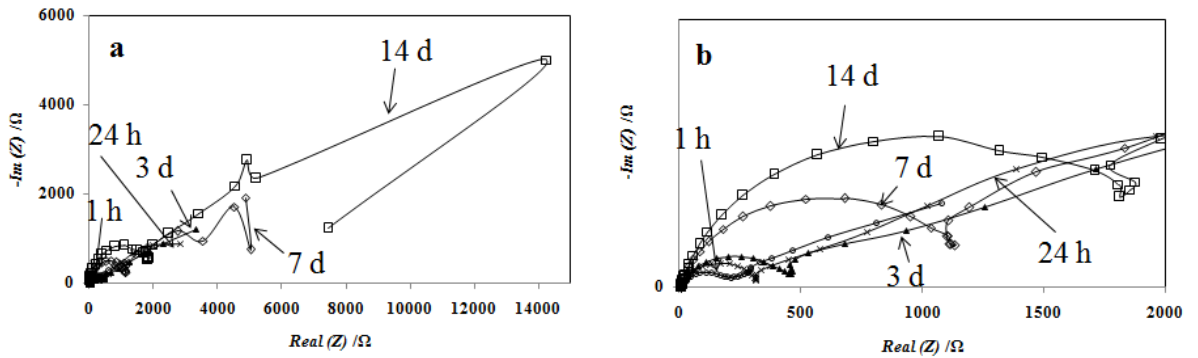
<i>Immersion time</i>	$R_s(\Omega)$	$R_t(\Omega/\text{cm}^2)$	$C_d(\mu\text{F}/\text{cm}^2)$
1h	70	154	201
24h	67	1616	136
3 days	59	2192	139
7 days	53	1898	230
14 days	53	2768	153

561

562

563

564



565

566 **Fig. 20.** (a) Nyquist plots of AlSi10Cu(Fe) sand cast aluminum alloy immersed in 3 wt. %
 567 NaCl solution after different immersion times

568

569

570 **Table 10.** Solution resistance (R_s), transfer resistance (R_t) and double layer capacitance (C_d)
 571 AlSi10Cu(Fe) sand cast aluminum alloy immersed in 3 wt. % NaCl solution after different
 572 immersion times.

573

<i>Immersion time</i>	$R_s(\Omega)$	$R_t(\Omega/\text{cm}^2)$	$C_d(\mu\text{F}/\text{cm}^2)$
1h	11	271	587
24h	12	260	613
3 days	9	542	407
7 days	7	1406	420
14 days	7	2536	323

574

575

576

Conclusions

577

578 The present work was performed to examine and to offer a better understanding of the
 579 influence of several intermetallics and porosities (nano and microporosities) on the corrosion
 580 behavior of AlSi10Cu(Fe) sand cast alloy containing zinc and to find the relationship between
 581 the microstructure and the corrosion behavior. Microstructure characterization and corrosion
 582 behavior of aluminum AlSi10Cu(Fe) sand cast alloy in chloride solution were investigated.
 583 The main results can be summarized as:

584 The chemical composition of the different second phases present in the alloy is variable,
585 several phases and a new phase $\text{Cu}_{61.22} \text{Zn}_{25.39} \text{Ni}_{11.85} \text{Al}_{1.54}$, white nanoparticles on a silicon
586 plate-like eutectic and coral-like eutectic have been observed.

587 Dissolution of aluminum phase surrounding the eutectic phases, and dissolution of fine
588 particles and/or segregation surrounding the β -Fe plates phases occur. Nanopores on the
589 surface of the samples have been characterized and can be responsible for the pitting
590 corrosion, and the analysis of pitting zones shows that the zones contain oxygen, aluminum,
591 silicon, magnesium, and chlorine.

592 The Nyquist plot evidences a charge resistance transfer at high frequency followed by a
593 diffusion phenomenon (Warburg line) at low frequency. Impedance measurements show
594 dissolution of metals on the alloy and electrolyte diffusion towards the porous surface layer of
595 alloy, without adsorption phenomenon. It can be assumed that the corrosion phenomena are
596 due to the appearance and the disappearance of porosities and the dissolution of less noble
597 elements.

598 The transfer resistance is about 2.7 k Ω in 0.3 wt. % NaCl and 2.5 k Ω in 3 wt. % NaCl
599 after two weeks of immersion, the double-layer capacitance is about 200 μF in the 0.3 wt. %
600 NaCl solution and 300 μF in 3 wt. % NaCl solution after 14 days of corrosion. An increase of
601 the transfer resistance and a change of the double layer capacitance with increasing immersion
602 duration were observed. The change of double layer capacitance can be due to the presence of
603 porosities on surface. The corrosion potential tends to -1.10 V after 14 days of corrosion in
604 0.3 and 3 wt. % NaCl solutions. The polarization resistance is about 2.8 k Ω in the 0.3 wt. %
605 NaCl solution, and 1.4 k Ω in the 3 wt. % NaCl solution. Due to its high corrosion rate value,
606 in the 3 wt. % NaCl solution, the use of the alloy in sea water is not recommended. Wide
607 passive windows, followed by the breakdown of passive film and excessive dissolution, were
608 observed in 0.3% and 3 wt. % NaCl solution.

References

609

610

611 Singh S, Goel DB (1990) Influence of thermomechanical ageing on tensile properties of 2014
612 aluminium alloy, *Journal of Materials Science* 25: 3894-3900.

613 <https://doi:10.1007/bf00582456>

614 Ahn SS, Pathan S, Koo JM, Baeg CH, Jeong CU, Son HT, Kim YH, Lee KH, Hong SJ (2018)
615 Enhancement of the Mechanical Properties in Al–Si–Cu–Fe–Mg Alloys with Various
616 Processing Parameters, *Materials* 11: 2150. <https://doi.org/10.3390/ma11112150>

617 Elzanaty H (2015) Effect of Composition on the Microstructure, Tensile and Hardness
618 Properties of Al–xSi alloys, *Journal of Materials Science & Surface Engineering* 2: 126-129.

619 Stadler F, Antrekowitsch H, Fragner W, Kaufmann H, Uggowitzer PJ (2011) The effect of Ni
620 on the high-temperature strength of Al-Si cast alloys *Materials Science Forum* 690: 274-277.

621 <https://doi.org/10.4028/www.scientific.net/MSF.690.274>

622 Stadler F, Antrekowitsch H, Fragner W, Kaufmann H, Uggowitzer PJ (2012) Effect of main
623 alloying elements on strength of Al–Si foundry alloys at elevated temperatures. *International*
624 *Journal of Cast Metals Research* 25: 215-224.

625 <https://doi.org/10.1179/1743133612Y.0000000004>

626 Ceschini L, Morri A, Morrin A, Toschi S, Johansson S, Seifeddine S (2015) Effect of
627 microstructure and overaging on the tensile behavior at room and elevated temperature of
628 C355-T6 cast aluminum alloy. *Materials & design* 83: 626-634.

629 <https://doi.org/10.1016/j.matdes.2015.06.031>

630 Zamani M, Seifeddine S, Jarfors AE (2015) High temperature tensile deformation behavior
631 and failure mechanisms of an Al–Si–Cu–Mg cast alloy—the microstructural scale effect.
632 *Materials & design* 86: 361. <https://doi.org/10.1016/j.matdes.2015.07.084>

633 Campbell J, *Castings* (2003) the new metallurgy of cast metals. 2nd Edition, Oxford.

634 Jiang W, Fan z, Dai T, Li C (2014) Effects of rare earth elements addition on microstructures,
635 tensile properties and fractography of A357 alloy. *Materials Science and Engineering A* 597:
636 237-244. <https://doi.org/10.1016/j.msea.2014.01.009>

637 Tenekedjiev N, Gruzleski JE (1990) Hypereutectic aluminium-silicon casting alloys—a
638 review, *Cast Metals* 3: 96-105. <https://doi.org/10.1080/09534962.1990.11819026>

639 Bogdanoff T, Seifeddine S, Dahle AK (2016) The effect of Si content on microstructure and
640 mechanical properties of Al-Si alloy. *La Metallurgia Italiana* 108: 65-69.

- 641 Barrirero J, Pauly C, Engstler, M, Ghanbaj J, Ghafoor N, Lin J, Schumacher P, Odén M,
642 Mücklich F (2019) Eutectic modification by ternary compound cluster formation in Al-Si
643 alloys, Scientific Reports 9. <https://doi:10.1038/s41598-019-41919-2>
- 644 Warmuzek M (2004) Aluminum-Silicon Casting Alloys: Atlas of Microfractographs, ASM
645 International Materials Park, Ohio, USA, ISBN: 978-0-87170-794-9.
- 646 Zazi N (2013) Effect of Heat Treatments on the Microstructure, Hardness and Corrosion
647 Behavior of Nondendritic AlSi9Cu3(Fe) Cast Alloy. Materials Science (Medziagotyra) 19:
648 258-263. <http://dx.doi.org/10.5755/j01.ms.19.3.1397>
- 649 Oya Y, Kojima Y, Hara N (2013) Influence of Silicon on Intergranular Corrosion for
650 Aluminum Alloys, Materials Transactions 54: 1200-1208.
651 <https://doi.org/10.2320/matertrans.M2013048>
- 652 Cáceres CH, Svensson IL, Taylor JA (2003) Strength-Ductility behaviour of Al-Si-Cu-Mg
653 casting alloy in T6 temper, International Journal of cast metals Research 15: 531-543.
654 <https://doi.org/10.1080/13640461.2003.11819539>
- 655 Ye HZ (2003) An overview of the development of Al-Si-Alloy based material for engine
656 applications, Journal of Materials engineering and Performance 12: 288-297.
657 <https://doi:10.1361/105994903770343132>
- 658 Ma P, Jia Y, Prashanth K, Yu Z, Li C, Zhao J, Yang S, Huang L (2017) Effect of Si content
659 on the microstructure and properties of Al-Si alloys fabricated using hot extrusion. Journal of
660 materials Research 32: 2210-2217. <https://doi:10.1557/jmr.2017.97>
- 661 Mohamed AMA, Samuel FHA (2012) review on the heat treatment of Al-Si-Cu/Mg casting
662 alloys, Heat Treatment-Conventional and Novel Applications; BOOK CHAPTER, InTech:
663 Rijeka, Croatia. <http://dx.doi.org/10.5772/79832>
- 664 Al-Hella, Kawther WA (2013) New approaches to casting hypereutectic Al-Si Alloys to
665 achieve simultaneous refinement of primary silicon and modification of eutectic silicon, a
666 thesis submitted for the degree of doctor of philosophy, Brunel center for advanced
667 solidification technology (BCAST), Brunel university.
- 668 Sjölander E, Seifeddine S (2010) The Heat Treatment of Al-Si-Cu-Mg Casting Alloys.
669 Journal of Materials Processing Technology 210: 1249-1259.
670 <https://doi.org/10.1016/j.jmatprotec.2010.03.020>

- 671 Dobkowska A, Adamczyk– Cieślak, Mizera, B., J, Kurzydłowski KJ, Kielbus A (2016) The
672 comparison of the microstructure and corrosion resistance of sand cast aluminum alloys,
673 Archives of Metallurgy and Materials 61: 209-212. <https://doi:10.1515/amm-2016-0038>.
- 674 Cecchel S, Cornacchia G, Gelfi, M (2017) Corrosion behavior of primary and secondary AlSi
675 high pressure die casting alloys, Materials and Corrosion 68: 961-669.
676 <https://doi:10.1002/maco.201709526>
- 677 Barr TL (1977) ESCA studies of naturally passivated metal foils, Journal of Vacuum Science
678 and Technology 14: 660-665. <https://doi:10.1116/1.569174>
- 679 Bessone JB, Salinas DR, Mayer Ebert CE, Lorenz WJ (1992) An EIS study of aluminium
680 barrier-type oxide films formed in different media, Electrochimica Acta 37: 2283-2290
681 [https://doi:10.1016/0013-4686\(92\)85124-4](https://doi:10.1016/0013-4686(92)85124-4)
- 682 Munoz AG, Bessone JB (1999) Pitting of aluminium in non-aqueous chloride media,
683 Corrosion Sciences 41: 1447-1463. [https://doi.org/10.1016/S0010-938X\(98\)00199-1](https://doi.org/10.1016/S0010-938X(98)00199-1)
- 684 Allachi H, Chaouket F, Draoui K (2010) Protection against corrosion in marine environments
685 of AA6060 aluminium alloy by cerium chlorides, Journal of Alloys and Compounds
686 491: 223-229. <https://doi.org/10.1016/j.jallcom.2009.11.042>
- 687 Zazi N, Bouabdallah A, Aaboubi O, Chopart, JP (2010) Pretreatment effects on the
688 electrochemical responses for aluminium–magnesium alloy AA5083 corrosion behavior,
689 Solid State Electrochemistry 14: 1705-1711. <https://doi:10.1007/s10008-010-1021-0>
- 690 Zaid B, Saidi D, Benzaid A, Hadji S (2008) Effects of pH and chloride concentration on
691 pitting corrosion of AA6061 aluminum alloy, Corrosion Sciences 50: 1841-1847.
692 <https://doi:10.1016/j.corsci.2008.03.006>
- 693 Djurdjevic M, Stockwell T, Sokolowski J (1999) The effect of strontium on the
694 microstructure of the aluminium–silicon and aluminium–copper eutectics in the 319
695 aluminium alloy, International Journal of Cast Metals Research 12: 67-73.
- 696 Samuel EH, Samuel AM, Doty HW (1997) Factors controlling the type and morphology of
697 Cu-containing phases in 319 Al alloy, Transactions of the American Foundry men's Society
698 30: 893-801.
699 <https://doi.org/10.1080/13640461.1999.11819344>
- 700 Li Z, Samuel AM, Samuel FH, Ravindran C, Valtierra S (2003) Effect of alloying elements
701 on the segregation and dissolution of Al₂Cu phase in Al–Si–Cu 319 alloys, Journal Materials
702 Sciences 38: 1203-1218. <https://doi:10.1023/A:1022857703995>

- 703 Dinnis CM, Taylor JA, Dahle AK (2006) Interactions between Iron, Manganese, and the Al-
704 Si Eutectic in Hypoeutectic Al-Si Alloys, Metallurgical and Materials Transactions A 37:
705 3283-3291. <https://doi:10.1007/BF02586163>
- 706 Ammar HR, Samiel AM, Samuel FA (2008) porosity and fatigue behavior of hypoeutectic
707 and hypereutectic aluminum-silicon casting alloy, International Journal of Fatigue 30: 1024-
708 1035. <https://doi.org/10.1016/j.ijfatigue.2007.08.012>
- 709 Ferreira IL, Lins JFC, Moutinho DJ, Gomes LG, Garcia A (2010) Numerical and
710 experimental investigation of microporosity formation in a ternary Al-Cu-Si alloy, Journal of
711 Alloys and Compounds 503: 31-39. <https://doi:10.1016/j.jallcom.2010.04.244>
- 712 Kuchariková L, Liptáková T, Tillová E, Bonek M, Medvecká D, (2020) Corrosion
713 behaviour correlation of the secondary aluminium casts in natural atmosphere and laboratory
714 conditions, Arch. Metall. Mater. 65: 1455-1462. <https://doi:10.24425/amm.2020.133713>
- 715 Michna S, Lukac I, Louda P, Ocenasek V, Schneider H, Drapala J, Koreny R, Miskufova A
716 (2007) Aluminum materials and technologies from A to Z, Adin, s.r.o.Presom, Czech
717 Republic.
- 718 Taylor JA, Metal-related castability effects in aluminium foundry alloys (1995) Cast Metals
719 8: 225-252. <https://doi.org/10.1080/09534962.1996.11819212>
- 720 Mbuya TO, Odera BO, Ng'ang'a SP (2003) Influence of iron on castability and properties of
721 aluminium silicon alloys: literature review, International Journal of Cast Metals Research 16:
722 451-465. <https://doi.org/10.1080/13640461.2003.11819622>
- 723 Roy N, Samuel AM, Samuel FH (1996) Porosity formation in Al-9 wt pct Si-3 wt pct Cu alloy
724 systems: Metallographic observations, Metallurgical and Materials Transactions A 27: 415-
725 429. <https://doi:10.1007/bf02648419>
- 726 Taylor JA (2004) The effect of iron in Al-Si casting alloys, 35th Australian Foundry Institute
727 National Conference, Adelaide, South Australia 148.
- 728 C. Berlanga-Labari, M. V. Biezma-Moraleda and Pedro J. Rivero, (2020) Corrosion of Cast
729 Aluminum Alloys: A Review, Metals, 10:1-29. [doi:10.3390/met10101384](https://doi.org/10.3390/met10101384).
- 730 Tillov E., Chalupov M, Hurtalov L (2012) Evolution of Phases in a Recycled Al-Si Cast
731 Alloy during Solution Treatment, Scanning Electron Microscopy 411.
732 <https://doi:10.5772/34542>
- 733 Mathers G (2002) The Welding of Aluminium and Its Alloys, Editor: Boca Raton, FL, CRC
734 Press; Cambridge, England.
- 735 Reardon AC (2011) Metallurgy for the Non-Metallurgist, Second Edition, Materials Park,
736 Ohio: ASM International.

- 737 Ambat R, Davenport AJ, Scamans GM, Afseth A (2006) Effect of iron-containing
738 intermetallic particles on the corrosion behaviour of aluminium, *Corrosion Science* 48: 3455-
739 3471. <https://doi.org/10.1016/j.corsci.2006.01.005>
- 740 McAlister AJ, Murray JL (1987) The (Al–Mn) Aluminum-Manganese system, *Journal of*
741 *Phase Equilibria*, 8: 438-447.
- 742 Bannour S, Abderrazak K, Mattei S, Masse JE, Autric M, Mhiri H (2013) The influence of
743 position in overlap joints of Mg and Al alloys on microstructure and hardness of laser welds,
744 *Journal Laser Applications* 25: 032001. <https://doi:10.2351/1.4792615>
- 745 Skoko Ž, Popović S, Štefanić G (2009) Microstructure of Al-Zn and Zn-Al Alloys, *Croatica*
746 *Chemica Acta* 82: 405-420.
- 747 Jia Q, Li D, Li S, Zhang Z, Zhang N (2018) High-Temperature Oxidation Resistance of NiAl
748 Intermetallic Formed In Situ by Thermal Spraying, *Coatings* 8: 292.
749 <https://doi.org/10.3390/coatings8080292>
- 750 Birbilis N, Buchheit RG (2005) Electrochemical Characteristics of Intermetallic Phases in
751 Aluminum Alloys, *Journal of The Electrochemical Society* 152: B140.
752 <https://doi:10.1149/1.1869984>
- 753 Kuchariková L, Liptáková T, Tillová E, Kajánek D, Schmidová E (2018) Role of Chemical
754 Composition in Corrosion of Aluminum Alloys, *Metals* 8: 581.
755 <https://doi.org/10.3390/met8080581>
- 756 Seri O, Furuya S, Soga N (1989) Effect of copper content on corrosion of aluminum, *Journal*
757 *of Japan Institute of Light Metals*, 39: 724-729. <https://doi:10.2464/jilm.39.724>
- 758 Hossain A, Gulshan F, Kurny ASW (2015) Electrochemical corrosion behavior of Ni-
759 containing hypoeutectic Al-Si alloy, *Journal of Electrochemical Science and Engineering* 5:
760 173-179. <https://doi.org/10.5599/jese.174>
- 761 Yoo YH, Park IJ, Kim JG, Kwak DH, Ji WS (2011) Corrosion characteristics of aluminum
762 alloy in bio-ethanol blended gasoline fuel: Part 1. The corrosion properties of aluminum alloy
763 in high temperature fuels, *Fuel* 90: 1208-1214.
764 <https://doi.org/10.1016/j.fuel.2010.10.058>
- 765 Pourbaix M (1974) *Atlas of Electrochemical Equilibria in Aqueous Solutions*, National
766 Association of Corrosion Engineers, Houston.
- 767 Rossi S, Eyraud M, Vacandio F, Massiani Y (2007) Corrosivity of long-term fire retardant
768 Fire Trol (R) 931 and Fire Foam (R) 103 on aluminium alloys and steel *Materials Chemistry*
769 *and Physics* 105: 260–267. [https://Doi: 10.1016/j.matchemphys.2007.04.055](https://Doi:10.1016/j.matchemphys.2007.04.055)

- 770 Frers SE, Stefenel MM, Mayer C, Chierchie T (1990) AC-Impedance measurements on
771 aluminium in chloride containing solutions and below the pitting potential, Journal of
772 Applied Electrochemistry 20: 996-999. <https://doi:10.1007/bf01019578>
- 773 Jafarzadeh K, Shahrabi T, Oskouei AA (2009) novel approach using EIS to study flow
774 accelerated pitting corrosion of AA5083-H321 aluminium- magnesium alloy in NaCl,
775 Journal of Applied Electrochemistry 39:1725–1731.
776 <https://Doi: 10.1007/s10800-009-9867-5>
- 777 Fernandes JCS, Travassos MA, Leitão E, Rangel CM, Barbosa M, Ferreira MGS (1989) the
778 influence of Li on the electrochemical behaviour of pure aluminium, portugaliae
779 electrochimica acta 7: 119-122.